
Accelerated Article Preview

Papain-like protease regulates SARS-CoV-2 viral spread and innate immunity

Received: 30 April 2020

Accepted: 23 July 2020

Accelerated Article Preview Published
online 29 July 2020

Cite this article as: Shin, D. et al. Papain-like protease regulates SARS-CoV-2 viral spread and innate immunity. *Nature* <https://doi.org/10.1038/s41586-020-2601-5> (2020).

Donghyuk Shin, Rukmini Mukherjee, Diana Grewe, Denisa Bojkova, Kheewoong Baek, Anshu Bhattacharya, Laura Schulz, Marek Widera, Ahmad Reza Mehdipour, Georg Tascher, Paul P. Geurink, Alexander Wilhelm, Gerbrand J. van der Heden van Noort, Huij Ovaa, Stefan Müller, Klaus-Peter Knobeloch, Krishnaraj Rajalingam, Brenda A. Schulman, Jindrich Cinatl, Gerhard Hummer, Sandra Ciesek & Ivan Dikic

This is a PDF file of a peer-reviewed paper that has been accepted for publication. Although unedited, the content has been subjected to preliminary formatting. Nature is providing this early version of the typeset paper as a service to our authors and readers. The text and figures will undergo copyediting and a proof review before the paper is published in its final form. Please note that during the production process errors may be discovered which could affect the content, and all legal disclaimers apply.

Papain-like protease regulates SARS-CoV-2 viral spread and innate immunity

<https://doi.org/10.1038/s41586-020-2601-5>

Received: 30 April 2020

Accepted: 23 July 2020

Published online: 29 July 2020

Donghyuk Shin^{1,2,3}, Rukmini Mukherjee^{1,2}, Diana Grewe², Denisa Bojkova⁴, Kheewoong Baek⁵, Anshu Bhattacharya^{1,2}, Laura Schulz⁶, Marek Widera⁴, Ahmad Reza Mehdipour⁶, Georg Tascher¹, Paul P. Geurink⁷, Alexander Wilhelm^{4,11}, Gerbrand J. van der Heden van Noort⁷, Huib Ovaa^{7,13}, Stefan Müller¹, Klaus-Peter Knobeloch⁸, Krishnaraj Rajalingam⁹, Brenda A. Schulman⁵, Jindrich Cinat⁴, Gerhard Hummer^{6,10}, Sandra Ciesek^{4,11,12} & Ivan Dikic^{1,2,3,12}✉

The papain-like protease PLpro is an essential coronavirus enzyme required for processing viral polyproteins to generate a functional replicase complex and enable viral spread^{1,2}. PLpro is also implicated in cleaving proteinaceous post-translational modifications on host proteins as an evasion mechanism against host anti-viral immune responses^{3–5}. Here, we provide biochemical, structural and functional characterization of the SARS-CoV-2 PLpro (SCoV2-PLpro) and outline differences to SARS-CoV PLpro (SCoV-PLpro) in controlling host interferon (IFN) and NF- κ B pathways. While SCoV2-PLpro and SCoV-PLpro share 83% sequence identity, they exhibit different host substrate preferences. In particular, SCoV2-PLpro preferentially cleaves the ubiquitin-like protein ISG15, whereas SCoV-PLpro predominantly targets ubiquitin chains. The crystal structure of SCoV2-PLpro in complex with ISG15 reveals distinctive interactions with the amino-terminal ubiquitin-like domain of ISG15, highlighting this high affinity and specificity. Furthermore, upon infection, SCoV2-PLpro contributes to the cleavage of ISG15 from interferon responsive factor 3 (IRF3) and attenuates type I interferon responses. Importantly, inhibition of SCoV2-PLpro with GRL-0617 impairs the virus-induced cytopathogenic effect, fosters the anti-viral interferon pathway and reduces viral replication in infected cells. These results highlight a dual therapeutic strategy in which targeting of SCoV2-PLpro can suppress SARS-CoV-2 infection and promote anti-viral immunity.

The novel coronavirus Severe Acute Respiratory Syndrome Coronavirus 2 (SARS-CoV-2) is the cause of the current worldwide outbreak of the respiratory disease COVID-19⁶. COVID-19 generally has less severe symptoms and a lower case-fatality rate, but is transmitted more rapidly compared to the related coronaviruses causing the Severe Acute Respiratory Syndrome (SARS) outbreak in 2003. The SARS-CoV-2 genome shares high sequence identity with SARS-CoV^{7,8}. Both viruses critically rely on the activity of viral proteases: the main protease (Mpro/3CLpro in non-structural protein 5 (nsp5)) and the papain-like protease (PLpro, a part of nsp3) to generate a functional replicase complex and enable viral spread^{1,2}. SCoV-PLpro also acts as a protease for ubiquitin and ISG15, known regulators of host innate immune pathways, and inhibition of SCoV-PLpro was shown to block SARS-CoV replication^{3–5}.

SARS-CoV-2 PLpro preferentially cleaves ISG15

While SCoV-PLpro and SCoV2-PLpro are closely related and distant from MERS-PLpro (Extended data Fig. 1a), purified SCoV-PLpro and

SCoV2-PLpro show differences in their substrate preferences, as revealed by their cleavage of ubiquitin or ISG15 from substrates in interferon (IFN- α)-treated HeLa cells (Extended data Fig. 1b). SCoV-PLpro strongly reduced the smears of ubiquitinated substrates, with a lesser effect on ISGylated substrates, whereas SCoV2-PLpro preferentially reduced ISGylation of substrates (Extended data Fig. 1b).

We next employed activity-based probes (ABPs), namely a propargylamide (Prg) warhead, which forms a covalent bond with catalytic cysteines, and a 7-amido-4-methylcoumarine (AMC) probe that is cleavable and concomitant with fluorescence emission thereby enabling the monitoring of protease activity kinetics^{9–13}. SCoV2-PLpro preferentially reacted with ISG15-Prg-probe, while showing weak activity towards K48-linked di-ubiquitin (K48-Ub₂) and Nedd8, and no activity towards SUMO-based Prg probes (Fig. 1a, Extended data Fig. 1c). The strongest reaction for SCoV-PLpro was observed with K48-Ub₂ Prg-probes, with less reactivity toward the ISG15 Prg-probe (Fig. 1a, Extended data Fig. 1c). This substrate preference was further confirmed

¹Institute of Biochemistry II, Faculty of Medicine, Goethe University, Theodor-Stern-Kai 7, 60590, Frankfurt am Main, Germany. ²Buchmann Institute for Molecular Life Sciences, Goethe University, Max-von-Laue-Str. 15, 60438, Frankfurt am Main, Germany. ³Max Planck Institute of Biophysics, Max-von-Laue-Str. 3, 60438, Frankfurt am Main, Germany. ⁴Institute of Medical Virology, University Hospital Frankfurt, Frankfurt am Main, Germany. ⁵Department of Molecular Machines and Signaling, Max Planck Institute of Biochemistry, Martinsried, Germany. ⁶Department of Theoretical Biophysics, Max Planck Institute of Biophysics, Max-von-Laue-Str. 3, 60438, Frankfurt am Main, Germany. ⁷Oncode Institute and Department of Chemical Immunology, Leiden University Medical Centre, Einthovenweg 20, 2333 ZC, Leiden, The Netherlands. ⁸Institute of Neuropathology, Faculty of Medicine, University of Freiburg, Freiburg, Germany. ⁹Cell Biology Unit, University Medical Center of the Johannes Gutenberg University Mainz, 55131, Mainz, Germany. ¹⁰Institute of Biophysics, Goethe University Frankfurt, Frankfurt am Main, Germany. ¹¹Institute of Pharmaceutical Biology, Goethe-University, Frankfurt/Main, Germany. ¹²Fraunhofer Institute for Molecular Biology and Applied Ecology (IME), Branch Translational Medicine and Pharmacology, Frankfurt, Germany. ¹³Deceased. ✉e-mail: dikic@biochem2.uni-frankfurt.de

using competition assays with increasing doses of K48-Ub₂ (Extended data Fig. 1d, e). In the reaction with SCoV-PLpro, K48-Ub₂ effectively competed with both ISG15-Prg or ISG15-AMC, while the competitive displacement was much less effective for SCoV2-PLpro. The catalytic efficiency (k_{cat}/K_M) of both PLpros was also examined (Fig. 1b, Extended data Table. 2) demonstrating that SCoV2-PLpro mediated AMC cleavage from ISG15-AMC was indeed better than from K48-Ub₂-AMC while SCoV-PLpro cleaved AMC from K48-Ub₂ more efficiently. Interestingly, in these assays the apparent catalytic efficiency (k_{cat}/K_M) of both PLpros towards ISG15 was similar, yet SCoV2-PLpro showed slightly higher ISG15 specificity (lower K_M , Fig. 1b, Extended data Table. 2). Consistently, SCoV2-PLpro displayed a 20-fold increase in ISG15 binding compared to K48-Ub₂, whereas SCoV-PLpro bound to K48-Ub₂ with a 10-fold higher affinity than ISG15 (Fig. 1c, Extended data Table. 3). In fact, the deISGylase activity of SCoV2-PLpro toward Prg- or AMC-based substrates, was similar to or higher than that of mouse USP18 (mUSP18), a specific deISGylase^{12,14} (Extended data Fig. 1f, g). A weak deneddylation activity was also observed for both PLpro enzymes towards hyperneddylated CUL1, a common feature for the *bona fide* deneddylase DEN1 (Extended data Fig. 1c, h, i). Taken together, these results indicate that SCoV2-PLpro preferentially cleaves ISG15 from substrates *in vitro* over ubiquitin chains and Nedd8, whereas SCoV-PLpro targets ubiquitin chains and to a lesser extent ISG15 and Nedd8 (Fig. 1d).

SCoV2-PLpro-ISG15 structural analysis

To gain insight into the molecular basis underlying SCoV2-PLpro-ISG15 specificity, we determined the crystal structure of a SCoV2-PLpro (C111S)-murine ISG15 complex (Fig. 2a, Extended data Fig. 2a). Notably, ISG15 displays two tandem ubiquitin-like folds. The overall assembly of SCoV2-PLpro and both ISG15 domains was similar to the MERS-PLpro-humanISG15 complex (PDB ID: 6BI8, Extended data Fig. 2a)¹⁵. The catalytic cysteine residue is also conserved in SARS (Extended data Fig. 2b). Compared to the crystal structure of ISG15 on its own (PDB ID: 5TLA)¹⁶, the N-terminal half of ISG15 is rotated by almost 90° and sits on the S2-helix of SCoV2-PLpro (Fig. 2b). The structure of SCoV-PLpro in complex with mISG15-C-term (PDB ID: 5TL7)¹⁶ showed that SCoV-PLpro and SCoV2-PLpro share the same binding mode to the C-lobe of mISG15 (Extended data Fig. 2c). We next compared the structure of the SCoV2-PLpro-ISG15 complex to that of SCoV-PLpro bound to K48-Ub₂, where the proximal ubiquitin is linked to the catalytic site. The major difference between the two complexes is an interaction remote from the catalytic site, with a protease S2 site binding the distal ubiquitin in the K48-linked chain, or the N-terminal ubiquitin-like fold in ISG15. While SCoV-PLpro Leu76 mediates a hydrophobic interaction with Ile44 on ubiquitin, the corresponding residue on SCoV2-PLpro is Thr75 (Fig. 2c). To mimic the hydrophobic interaction observed in SCoV-PLpro, we generated two variants of SCoV2-PLpro (T75A and T75L). Interestingly, the T75L mutant resulted in a K48-Ub₂-AMC cleavage, while T75A did not (Figure. 2d). This indicates that a properly sized hydrophobic residue at this site is a critical determinant for ubiquitin binding. We also compared papain-like proteases (PLP) from other coronaviruses including common human coronaviruses OC43, 229E and NL63 (Extended data Fig. 3). Intriguingly, the S2-binding site in PLPs is the poorly conserved across coronaviruses and showed variability of hydrophobicity at the position corresponding to Thr75 of SCoV2-PLpro, which might influence substrate specificity.

Next, we examined if other SCoV2-PLpro residues contribute to its enhanced ISG15 affinity. SCoV2-PLpro Val66 faces the hydrophobic patch (Ala2, Thr20, Met23) on ISG15 N-terminal ubiquitin fold domain (Fig. 2e). Intriguingly, both PLpro enzymes share Phe (SCoV2-PLpro Phe69 and SCoV-PLpro Phe70) as the core residue mediating hydrophobic interactions with either ubiquitin or ISG15. Mutating Phe69 (F69A) or Val66 (V66A) on SCoV2-PLpro significantly decreased its enzymatic activity and showed slower reaction with ISG15-Prg compared to the wild type (Fig. 2f).

The interaction between SCoV2-PLpro and K48-Ub₂ and mISG15 was also examined using molecular dynamics (MD) simulations (Extended data Fig. 2d, 2e). Multi-microsecond MD simulations confirmed that SCoV2-PLpro interacts more tightly with ISG15 compared to K48-Ub₂ (reconfirming K_d values measured in Fig. 1e). In three independent runs of 3.2 μ s each, mISG15 remained bound as in the SCoV2-PLpro:mISG15 X-ray structure. In contrast, the distal ubiquitin of K48-Ub₂ separated from SCoV2-PLpro in four out of six runs on a microsecond time scale. We identified L75T to be the difference between SCoV2-PLpro and SCoV-PLpro, as it weakens the hydrophobic cluster within the binding interface. We observed that water transiently enters between Ile44^{Ub} and Thr75^{CoV2} prior to dissociation. Indeed, in simulations of the SCoV-PLpro double mutant (S67V/L76T) with K48-Ub₂, a similar water-mediated dissociation mechanism was observed (Extended data Fig. 2f, g). Together, these results suggest that the S2 region determines substrate specificity and that SCoV2-PLpro has relative preference toward ISG15.

GRL-0617 is an inhibitor of SCoV2-PLpro

With the pressing urgency to identify novel therapeutic strategies against COVID-19, we tested the effect of GRL-0617, a non-covalent inhibitor of SCoV-PLpro on SCoV2-PLpro (Fig. 3a)¹⁷. GRL-0617 is a naphthalene-based inhibitor developed against SCoV-PLpro and does not inhibit other host proteases^{17,18}. Based on the binding mode of GRL-0617 and other known naphthalene inhibitors to SCoV-PLpro¹⁷⁻²⁰, we postulated that the conserved Tyr268 of SCoV2-PLpro could also bind GRL-0617 and block the entry of the ISG15 C-terminus toward the protease catalytic cleft (Fig. 3b, Extended data Fig. 4a-c). Indeed, the IC_{50} of GRL-0617 to SCoV2-PLpro was similar to that of SCoV-PLpro (Fig. 3c, Extended data Fig. 4d, e). Interestingly, this inhibitor is ineffective against MERS-PLpro²¹. We hypothesized that this could be due to the presence of Thr instead of Tyr at this conserved position (Extended data Fig. 3a). Accordingly, the mutation of Tyr268 to either Thr(Y269T) or Gly(Y268G) in SCoV2-PLpro strongly reduced the inhibitory effect of GRL-0617 (Fig. 3c, Extended data Fig. 4d, e), indicating the critical role of Tyr268 in this process. MD simulations of GRL-0617 with SCoV-PLpro and SCoV2-PLpro further confirmed a common binding mode between GRL-0617 and Tyr268 (Tyr269 for SARS) (Extended data Fig. 4b, c).

To assess the therapeutic value of GRL-0617 against COVID-19 we tested the effect of GRL-0617 on the SCoV2-PLpro deISGylase or deubiquitinase activities of host proteins. GRL-0617 effectively blocked SCoV2-PLpro leading to increased levels of ISGylated proteins in IFN- α treated cell lysates (Extended data Fig. 4f). GRL-0617 also blocked the deubiquitination activity of SCoV-PLpro (Extended data Fig. 4f). Intriguingly, the effects of GRL-0617 on the reaction between Prg-probes with SCoV2-PLpro were more prominent with ISG15_{C-term}-Prg than ISG15_{FL}-Prg or ubiquitin versus K48-Ub₂ to SCoV-PLpro (Extended data Fig. 4g, h), consistent with the structural data indicating that the interaction between ISG15 N-terminal ubiquitin-fold domain potentiates the interaction with SCoV2-PLpro. These results showed that GRL-0617 inhibits both SCoV2-PLpro and SCoV-PLpro.

PLpro regulates IFN and NF- κ B pathways

To understand the differences in the pathophysiological roles of SCoV2-PLpro and SCoV-PLpro, and to expand our knowledge of the SARS-CoV-2 protein interaction map²², we analysed the cellular interactome of both proteins. ISG15 is significantly enriched in complexes with a catalytically inactive version of SCoV2-PLpro (C111S), whereas a SCoV-PLpro mutant (C111S) predominantly associated with ubiquitin (Fig 4a, b). In mammalian cells treated with type I IFNs (ISRE-promoter dependent, IFN- α), immunoprecipitation of unconjugated ISG15 and ISG15-positive smears, likely representing ISGylated substrates, was more pronounced with GFP-SCoV2-PLpro (C111S) than

with GFP-SCoV-PLpro (C111S) (Fig 4c). This association was blocked upon GRL-0617 treatment (Fig 4c). Moreover, these closely related PLpro enzymes associate with distinct and specific sets of host proteins (Fig. 4a). For SCoV2-PLpro, these include PRKDC that is related to type I interferon induction²³; heterogenous nuclear ribonucleoprotein K (HNRNPK) involved in splicing of the host RNA, a process essential for SARS-CoV-2 replication in cells²⁴; and Galectin1, which can induce viral fusion with target cells during HIV infection²⁵ (Fig. 4a). In contrast, SCoV-PLpro strongly associates with several serine protease inhibitors (serpins), including SERPIN B3, proposed to inhibit papain proteases^{26,27}. Interestingly, expression of SERPIN B3 together with PLpro enzymes partially restored NF- κ B signalling in cells expressing SCoV-PLpro, but had no effect on SCoV2-PLpro regulation of the IFN pathway (Extended data Fig. 5a, b).

Consistently, expression of SCoV2-PLpro and SCoV-PLpro in mammalian cells decreased ISGylation of cellular proteins following IFN- α stimulation (Extended data Fig. 5c), including that of interferon regulatory factor 3 (IRF3), a critical component in the type I interferon pathway²⁸. Both SCoV2-PLpro and SCoV-PLpro caused the loss of IRF3 ISGylation, with SCoV2-PLpro having a much stronger effect (Fig. 4d). A decrease in phosphorylation of TBK1, IRF3 and nuclear translocation of IRF3 was detected upon SCoV-PLpro or SCoV2-PLpro expression (Extended data Fig. 5d, e). The SCoV2-PLpro catalytic mutant (C111S) showed stronger dominant negative effects on IRF3 phosphorylation compared to the SCoV-PLpro catalytic mutant (C111S) (Extended data Fig. 5d, e). TBK1 phosphorylation also activates the NF- κ B pathway causing upregulation of inflammatory signalling²⁹. Although the expression of SCoV-PLpro had less impact on IRF3 ISGylation (Fig. 4d), it strongly attenuated degradation of I κ B- α (Extended data Fig. 5f, g). SCoV-PLpro also caused a severe reduction in nuclear translocation of p65 in TNF- α treated cells (Extended data Fig. 5h).

Sensing of viral nucleic acids is mimicked by poly (I:C) treatment, which induces IFN- β expression³⁰. Expression of SCoV2-PLpro more effectively decreased the level of IFN- β promoter activation compared to SCoV-PLpro following poly (I:C) treatment. This inhibitory effect of both PLpro enzymes was neutralized by GRL-0617 treatment (Extended data Fig. 6a, 6c). By contrast, expression of SCoV-PLpro predominantly blocked the TNF- α -induced NF- κ B-p65 expression, which was also sensitive to GRL-0617 treatment (Extended data Fig. 6b, 6d). Together, we show how two closely related coronaviruses (SARS and SARS-CoV-2) differentially counteract the host immune system using their PLpro enzymes.

PLpro inhibition affects viral spread and IFN responses

It has been shown that GRL-0617 inhibits viral replication of SARS-CoV¹⁷. Thus, to determine whether inhibiting SCoV2-PLpro can also block SARS-CoV-2 replication, CaCo-2 cells were infected with SARS-CoV-2 and treated with GRL-0617 (Fig. 5a). The effect of GRL-0617 was measured by cytopathogenic effect (CPE) inhibition. We observed a gradual dose-dependent inhibition of SARS-CoV-2-induced CPE in the presence of GRL-0617 with 100 μ M of GRL-0617 showing nearly a 100% CPE inhibitory effect (Fig. 5b). In addition, GRL-0617 treatment reduced the active viral replication (SARS-CoV-2 subgenomic RNA4 encoding E gene), measured by genetic monitoring of the intracellular production of viral RNA (Fig. 5c). Consequently, a decrease in the release of viral particles from infected cells into the supernatant was also observed upon GRL-0617 treatment (Fig. 5d, Extended data Fig. 7a, respectively). This suggests that GRL-0617 mediated inhibition of SCoV2-PLpro impedes the viral replication thereby attenuating the on-going viral RNA synthesis.

Having demonstrated a role for SCoV2-PLpro and SCoV-PLpro expression in dampening host anti-viral IFN pathways, we anticipated that GRL-0617 inhibition could also reverse this process. Indeed, GRL-0617 treatment of SARS-CoV-2-infected cells led to a significant increase in IRF3 ISGylation (Fig. 5e), which has previously been shown to regulate

anti-viral immune response³¹. Moreover, phosphorylation of IRF3 and TBK1, markers for IFN pathway activation, and p65 phosphorylation, used to monitor NF- κ B pathway activation, were all increased in SARS-CoV-2-infected cells upon GRL-0617 treatment (Fig 5f). Importantly, GRL-0617 treatment significantly rescued the expression level of IFN-responsive genes (ISG15, OAS1, PKR, MX1) in SARS-CoV-2 infected cells (Fig. 5g, Extended data Fig. 7b). These findings provide evidence that inhibition of SCoV2-PLpro, in addition to blocking viral RNA synthesis, can also increase anti-viral signalling via TBK1 and IRF3 (Extended data Fig. 7c). While experiments conducted with GRL-0617 provide evidence supporting the therapeutic value of pharmacologically targeting SCoV2-PLpro in patients, given its low potency, additional studies are needed in order to develop more potent and selective PLpro inhibitors.

Finally, we tested changes in CaCo-2 cells upon SARS-CoV and SARS-CoV-2 infection. GRL-0617 treatment of infected cells had an overall similar pattern in biochemical and transcriptional parameters of the type I IFN and NF- κ B pathways (Fig. 5e–g). Interestingly, however, we found that GRL-0617 was consistently more effective in restoring the ISGylation and phosphorylation level of IRF3, and on the expression of IFN responsive genes upon SARS-CoV-2 infection compared to SARS-CoV (Fig. 5e–g). In contrast, transcription levels of the proinflammatory cytokines IL-6 and IL-8 appeared similar between SARS-CoV and SARS-CoV-2 in this epithelial cell culture models (Fig 5g). Consistent with these observations, a recent study has shown that SARS-CoV-2 infection, in animal models and COVID-19 patients, is correlated with low IFN type I and type III responses³². Even though preferential activity of SCoV2-PLpro towards deISGylation may contribute to decreased type I IFN signalling, more detailed studies are needed to understand key regulatory factors contributing to innate and adaptive immunity that control distinct pathologic outcomes of SARS-CoV and SARS-CoV-2 infections³³.

Taken together, this interdisciplinary study provides mechanistic understanding of SCoV2-PLpro functions during SARS-CoV-2 infection and establishes SCoV2-PLpro as a promising target for therapeutic intervention against COVID-19. Recent reports of newly identified inhibitors of SCoV2-PLpro^{34–36} may lead to a rapid development of novel anti-COVID-19 therapeutics with a dual effect – blocking SARS-CoV-2 spread and promoting anti-viral immunity in the host. Also, the main protease of SARS-CoV-2 has been in the focus as a potential drug target against COVID-19 and several novel inhibitors have already been described^{37–39}. Combining drugs targeting essential SARS-CoV-2 proteases (PLpro and/or main protease) and drugs targeting SARS-CoV-2 RNA-dependent polymerase may offer successful therapeutic options in the future⁴⁰.

Online content

Any methods, additional references, Nature Research reporting summaries, source data, extended data, supplementary information, acknowledgements, peer review information; details of author contributions and competing interests; and statements of data and code availability are available at <https://doi.org/10.1038/s41586-020-2601-5>.

1. Harcourt, B. H. et al. Identification of Severe Acute Respiratory Syndrome Coronavirus Replicase Products and Characterization of Papain-Like Protease Activity. *J. Virol.* **78**, 13600–13612 (2004).
2. Lim, K. P., Ng, L. F. P. & Liu, D. X. Identification of a Novel Cleavage Activity of the First Papain-Like Proteinase Domain Encoded by Open Reading Frame 1a of the Coronavirus Avian Infectious Bronchitis Virus and Characterization of the Cleavage Products. *J. Virol.* **74**, 1674–1685 (2000).
3. Frieman, M., Ratia, K., Johnston, R. E., Mesecar, A. D. & Baric, R. S. Severe Acute Respiratory Syndrome Coronavirus Papain-Like Protease Ubiquitin-Like Domain and Catalytic Domain Regulate Antagonism of IRF3 and NF- κ B Signaling. *J. Virol.* **83**, 6689–6705 (2009).
4. Devaraj, S. G. et al. Regulation of IRF-3-dependent Innate Immunity by the Papain-like Protease Domain of the Severe Acute Respiratory Syndrome Coronavirus. *J. Biol. Chem.* **282**, 32208–32221 (2007).

5. Bailey-Elkin, B. A. *et al.* Crystal Structure of the Middle East Respiratory Syndrome Coronavirus (MERS-CoV) Papain-like Protease Bound to Ubiquitin Facilitates Targeted Disruption of Deubiquitinating Activity to Demonstrate Its Role in Innate Immune Suppression. *J. Biol. Chem.* **289**, 34667–34682 (2014).
6. Huang, C. *et al.* Clinical features of patients infected with 2019 novel coronavirus in Wuhan, China. *Lancet* **395**, 497–506 (2020).
7. Lu, R. *et al.* Genomic characterisation and epidemiology of 2019 novel coronavirus: implications for virus origins and receptor binding. *Lancet* **395**, 565–574 (2020).
8. Zhou, P. *et al.* A pneumonia outbreak associated with a new coronavirus of probable bat origin. *Nature* **579**, 270–273 (2020).
9. Sommer, S., Weikart, N. D., Linne, U. & Mootz, H. D. Covalent inhibition of SUMO and ubiquitin-specific cysteine proteases by an in situ thiol-alkyne addition. *Bioorg. Med. Chem.* **21**, 2511–2517 (2013).
10. Ekkebus, R. *et al.* On Terminal Alkynes That Can React with Active-Site Cysteine Nucleophiles in Proteases. *J. Am. Chem. Soc.* **135**, 2867–2870 (2013).
11. Flierman, D. *et al.* Non-hydrolyzable Diubiquitin Probes Reveal Linkage-Specific Reactivity of Deubiquitylating Enzymes Mediated by S2 Pockets. *Cell Chem. Biol.* **23**, 472–482 (2016).
12. Basters, A. *et al.* Structural basis of the specificity of USP18 toward ISG15. *Nat. Struct. Mol. Biol.* **24**, 270–278 (2017).
13. Geurink, P. P. *et al.* Profiling DUBs and Ubl-specific proteases with activity-based probes. in *Methods in Enzymology* 357–387 (2019). <https://doi.org/10.1016/bs.mie.2018.12.037>.
14. Basters, A. *et al.* Molecular characterization of ubiquitin-specific protease 18 reveals substrate specificity for interferon-stimulated gene 15. *FEBS J.* **281**, 1918–1928 (2014).
15. Clasman, J. R., Everett, R. K., Srinivasan, K. & Mesecar, A. D. Decoupling deISGylating and deubiquitinating activities of the MERS virus papain-like protease. *Antiviral Res.* **174**, 104661 (2020).
16. Daczkowski, C. M. *et al.* Structural Insights into the Interaction of Coronavirus Papain-Like Proteases and Interferon-Stimulated Gene Product 15 from Different Species. *J. Mol. Biol.* **429**, 1661–1683 (2017).
17. Ratia, K. *et al.* A noncovalent class of papain-like protease/deubiquitinase inhibitors blocks SARS virus replication. *Proc. Natl. Acad. Sci.* **105**, 16119–16124 (2008).
18. Báez-Santos, Y. M. *et al.* X-ray Structural and Biological Evaluation of a Series of Potent and Highly Selective Inhibitors of Human Coronavirus Papain-like Proteases. *J. Med. Chem.* **57**, 2393–2412 (2014).
19. Ghosh, A. K. *et al.* Severe Acute Respiratory Syndrome Coronavirus Papain-like Novel Protease Inhibitors: Design, Synthesis, Protein-Ligand X-ray Structure and Biological Evaluation. *J. Med. Chem.* **53**, 4968–4979 (2010).
20. Ghosh, A. K. *et al.* Structure-Based Design, Synthesis, and Biological Evaluation of a Series of Novel and Reversible Inhibitors for the Severe Acute Respiratory Syndrome-Coronavirus Papain-Like Protease. *J. Med. Chem.* **52**, 5228–5240 (2009).
21. Kilianski, A. & Baker, S. C. Cell-based antiviral screening against coronaviruses: Developing virus-specific and broad-spectrum inhibitors. *Antiviral Res.* **101**, 105–112 (2014).
22. Gordon, D. E. *et al.* A SARS-CoV-2 protein interaction map reveals targets for drug repurposing. *Nature* (2020) <https://doi.org/10.1038/s41586-020-2286-9>.
23. Ferguson, B. J., Mansur, D. S., Peters, N. E., Ren, H. & Smith, G. L. DNA-PK is a DNA sensor for IRF-3-dependent innate immunity. *Elife* **1**, e00047 (2012).
24. Bojkova, D. *et al.* Proteomics of SARS-CoV-2-infected host cells reveals therapy targets. *Nature* (2020) <https://doi.org/10.1038/s41586-020-2332-7>.
25. Ouellet, M. *et al.* Galectin-1 Acts as a Soluble Host Factor That Promotes HIV-1 Infectivity through Stabilization of Virus Attachment to Host Cells. *J. Immunol.* **174**, 4120–4126 (2005).
26. Schick, C. *et al.* Cross-Class Inhibition of the Cysteine Proteinases Cathepsins K, L, and S by the Serpin Squamous Cell Carcinoma Antigen 1: A Kinetic Analysis †. *Biochemistry* **37**, 5258–5266 (1998).
27. Takeda, A., Yamamoto, T., Nakamura, Y., Takahashi, T. & Hibino, T. Squamous cell carcinoma antigen is a potent inhibitor of cysteine proteinase cathepsin L. *FEBS Lett.* **359**, 78–80 (1995).
28. Stetson, D. B. & Medzhitov, R. Type I Interferons in Host Defense. *Immunity* **25**, 373–381 (2006).
29. Liu, T., Zhang, L., Joo, D. & Sun, S.-C. NF-κB signaling in inflammation. *Signal Transduct. Target. Ther.* **2**, 17023 (2017).
30. Sheikh, F., Dickensheets, H., Gamero, A. M., Vogel, S. N. & Donnelly, R. P. An essential role for IFN-β in the induction of IFN-stimulated gene expression by LPS in macrophages. *J. Leukoc. Biol.* **96**, 591–600 (2014).
31. Shi, H.-X. *et al.* Positive Regulation of Interferon Regulatory Factor 3 Activation by Herc5 via ISG15 Modification. *Mol. Cell. Biol.* **30**, 2424–2436 (2010).
32. Blanco-Melo, D. *et al.* Imbalanced Host Response to SARS-CoV-2 Drives Development of COVID-19. *Cell* **181**, 1036–1045.e9 (2020).
33. Niemeyer, D. *et al.* The papain-like protease determines a virulence trait that varies among members of the SARS-coronavirus species. *PLoS Pathog.* **14**, e1007296 (2018).
34. Anson, B. J. *et al.* Broad-spectrum inhibition of coronavirus main and papain-like 2 proteases by HCV drugs. *Res. Sq.* (2020) <https://doi.org/10.21203/rs.3.rs-26344/v1>.
35. Shanker, A. K., Bhanu, D., Alluri, A. & Gupta, S. Whole-genome sequence analysis and homology modelling of the main protease and non-structural protein 3 of SARS-CoV-2 reveal an aza-peptide and a lead inhibitor with possible antiviral properties. *New J. Chem.* **44**, 9202–9212 (2020).
36. Rut, W. *et al.* Activity profiling and structures of inhibitor-bound SARS-CoV-2-PLpro protease provides a framework for anti-COVID-19 drug design. *bioRxiv* (2020) <https://doi.org/10.1101/2020.04.29.068890>.
37. Zhang, L. *et al.* Crystal structure of SARS-CoV-2 main protease provides a basis for design of improved α-ketoamide inhibitors. *Science* (80-.). **368**, 409–412 (2020).
38. Jin, Z. *et al.* Structure of Mpro from COVID-19 virus and discovery of its inhibitors. *Nature* (2020) <https://doi.org/10.1038/s41586-020-2223-y>.
39. Dai, W. *et al.* Structure-based design of antiviral drug candidates targeting the SARS-CoV-2 main protease. *Science* (80-.). **eabb4489**, (2020).
40. Lo, H. S. *et al.* Simeprevir suppresses SARS-CoV-2 replication and synergizes with remdesivir. *bioRxiv* (2020) <https://doi.org/10.1101/2020.05.26.116020>.

Publisher's note Springer Nature remains neutral with regard to jurisdictional claims in published maps and institutional affiliations.

© The Author(s), under exclusive licence to Springer Nature Limited 2020

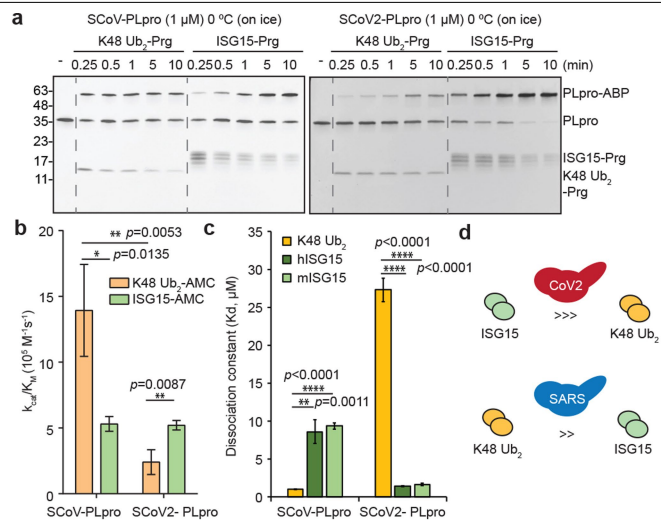


Fig. 1 | DeISGylating and Deubiquitinating activities of SCoV-PLpro and SCoV2-PLpro. **a**, SCoV-PLpro (left) or SCoV2-PLpro (right) were incubated with indicated Prg-probes for indicated time points. Experiments were repeated three times independently with similar results. **b**, Catalytic efficiency (k_{cat}/K_M) of SCoV2-PLpro and SCoV-PLpro on K48-Ub₂-AMC or ISG15-AMC cleavage. **c**, Dissociation constant (Kd) of SCoV2-PLpro and SCoV-PLpro. Data in **c**, **d** were presented as mean \pm S.D or mean \pm S.E.M, respectively (n=3, independent experiments). * $p < 0.05$, ** $p < 0.01$, **** $p < 0.0001$; two-tailed paired t-tests. **d**, Schematic representation of substrate specificity of SCoV2-PLpro and SCoV-PLpro.

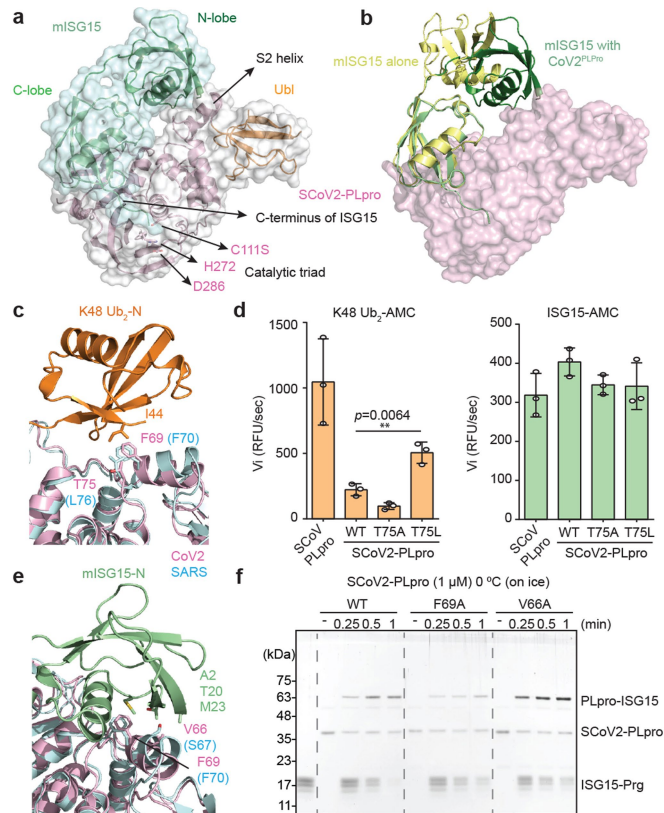


Fig. 2 | Structural analysis of SARS-CoV-2 PLpro in complex with full length ISG15. **a**, Crystal structure of SARS-CoV-2 PLpro^{C1115} in complex with murine ISG15 (mISG15). C-terminal glycine of mISG15 and catalytic triad of SCoV2-PLpro are highlighted as stick model. Ubiquitin like domain (Ubl) are coloured in orange. **b**, Comparison of unbound form of mISG15 with mISG15 in complex with SCoV2-PLpro. **d**, Initial velocity of AMC release from AMC-probes (K48-Ub₂-AMC, ISG15-AMC) with indicated PLpro and its mutants are presented as mean ± S.D (n=3, independent experiments). ***p* < 0.01; two-tailed paired t-tests. **e**, Comparison of K48-Ub₂:SCoV-PLpro complex structure (PDB ID: 5E6j) with mISG15:SCoV2-PLpro. Residues forming hydrophobic interactions are highlighted as stick model. **f**, ISG15-Prg were incubated with SCoV2-PLpro wild type and its mutants for indicated time points. Experiments were repeated three times independently with similar results.

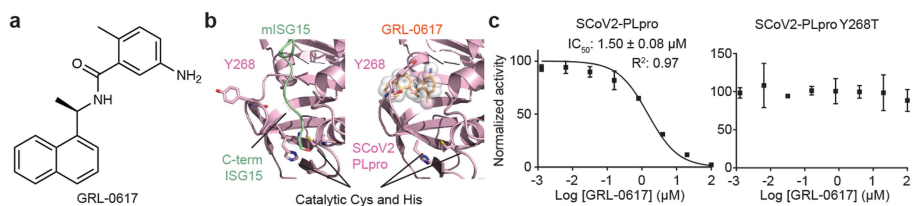


Fig. 3 | Effect of GRL-0617 inhibitor on SCoV2-PLpro. **a**, Structure of GRL-0617. **b**, Comparison of ISG15-bound (left) and GRL-0617 bound (right) structure. The blocking loop 2 (BL2 loop) of SCoV2-PLpro is modelled based on GRL-0617 bound SCoV-PLpro and SCoV2-PLpro structures (PDBID: 3E9S¹⁷,

6W9C). GRL-0617-interacting Tyr268 and catalytic Cys, His residues are highlighted as stick model. **c**, Cleavage of ISG15-AMC was measured and normalized to DMSO control. IC₅₀ of GRL-0617 to SCoV2-PLpro are presented. Data are presented as mean ± S.D (n=3, independent experiments).

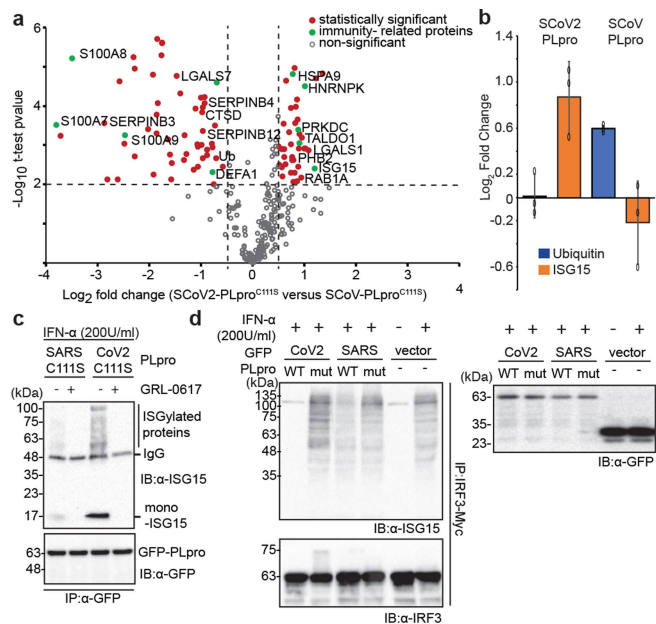


Fig. 4 | Effect on PLpros on IFN and NF- κ B pathways. **a**, Interactome analysis of SCoV2-PLpro C111S/SCoV-PLpro C111S. Statistically significant- and immunity-related- proteins are highlighted. **b**, Log₂ fold change of ubiquitin and ISG15 from SCoV2-PLpro or SCoV-PLpro versus empty vector. Data are presented as mean \pm S.D (n=3, independent experiments). **c**, ISGylated proteins were enriched from IFN- α treated A549 cells by indicated PLPro. **d**, ISGylation level of Myc-IRF3 was examined from A549 cells expressing indicated GFP-PLpros. Experiments in **c**, **d** were repeated three times independently with similar results.

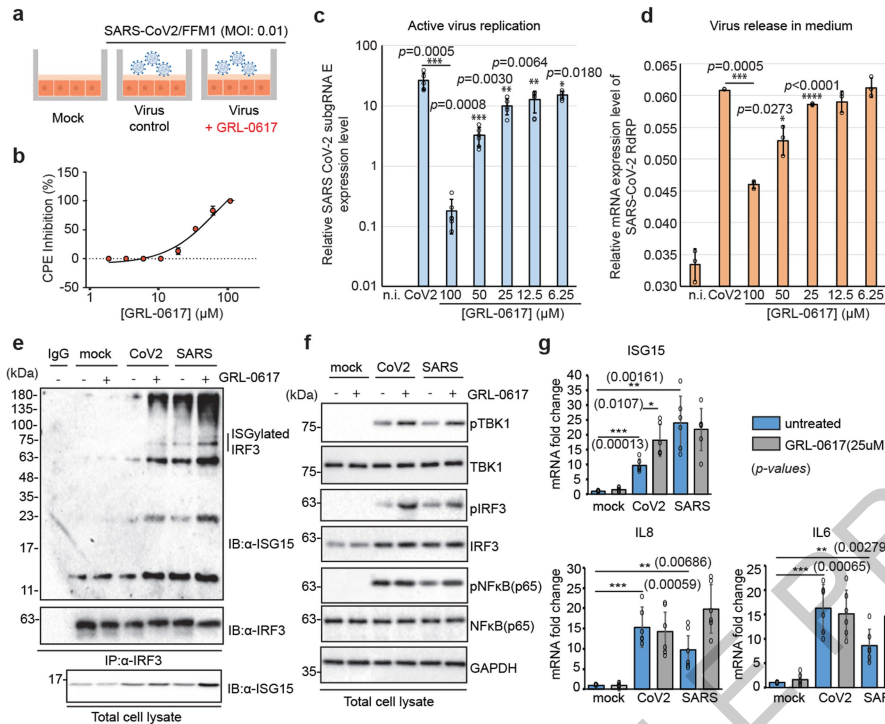


Fig. 5 | Inhibitory effects of GRL-0617 on SARS-CoV2. **a**, Schematic representation of SARS-CoV-2 growth inhibition test with GRL-0617. **b**, CPE inhibition rate of GRL-0617 on SARS-CoV2 infected CaCo-2 cells. **c**, Intracellular active virus replication was analysed by measuring SARS-CoV-2 subgenomic RNA (subgRNA E) level and normalized to cellular actin level. **d**, Release of viral particles in culture medium was analysed by PCR targeting the open reading frame for RNA dependent RNA polymerase (RdRp) of SARS-CoV-2. **e**, **f**, The effect of GRL-0617 on type I IFN-pathway. CaCo-2 cells were infected with

SARS-CoV-2 or SARS with or without GRL-0617 (50 μM). **e**, Endogenous IRF3 was immunoprecipitated and analysed by immunoblotting. **f**, Phosphorylation of TBK1 level were analysed by immunoblotting. **g**, Relative mRNA-levels of indicated genes from infected cells with or without treatment of GRL-0617 (25 μM) were analysed and normalized to 18S. Data in **c**, **d**, **g** are presented as mean ± S.D (n=3, independent experiments). **p* < 0.05, ***p* < 0.01, ****p* < 0.001, *****p* < 0.0001; two-tailed paired t-tests. Experiments in **e**, **f** were repeated three times independently with similar results.

Article

Methods

Plasmids construction

The papain-like protease domain sequence is obtained from SARS-CoV-2 complete genome (NCBI genome databank, [Severe acute respiratory syndrome coronavirus 2 isolate Wuhan-Hu-1, complete genome; NC_045512](#)). Protein sequence for CoV2 PLpro-Ubl domain (amino acids, 746-1060) of Nsp3 protein from SARS-CoV-2 ([Nsp3; YP_009725299.1](#)) was codon optimized, synthesized and cloned into pET28b with NcoI and XhoI to have C-terminal His-tag (Genescript). Protein sequences of PLpro-Ubl domain of SARS and MERS from (PDB ID: 3MJ5, 5W8U, respectively)^{19,41} were also codon optimized, synthesized and cloned into pET28b with NcoI and XhoI to have C-terminal His-tag (Genescript). Mutants were generated by PCR and verified by sequencing. For mammalian expression, PLpros are cloned into pEGFP-C1 (clontech). To produce the vector pACE-ISG15, a synthetic cDNA was used for murine ISG15 (Residues 1-155) and an N-terminal His6-Tag and the recognition site for the HRV-3C protease coded, ordered from Mr. Gene (Regensburg, Germany)

Protein purification

BL21(DE3) E. coli competent cells (NEB) were transformed with plasmids and grown in LB medium to an OD₆₀₀ of 0.6-0.8 at 37 °C. Protein production was induced by addition of 0.5 mM IPTG (isopropyl D-thiogalactopyranoside) and 1 mM Zinc Chloride (ZnCl₂) the cells were further grown overnight at 18 °C and harvested. The cell pellet was resuspended in lysis buffer (50 mM Tris-HCl, 150 mM NaCl, 10 mM Imidazole, 2 mM DTT, pH 8.5) and lysed by sonication and centrifuged at 13,000 rpm to clarify the supernatant. The supernatant was incubated 2 hours with TALON beads (Takara) pre-equilibrated with lysis buffer and non-specific proteins were cleared with washing. Proteins were eluted with elution buffer (50 mM Tris-HCl, 150 mM NaCl, 250 mM Imidazole, 2 mM DTT, pH 8.5). Eluted proteins were buffer exchanged to storage buffer (20 mM Tris-HCl, 100 mM NaCl, 2 mM DTT, pH 8.5) and stored for biochemical analysis. For crystallization of SCoV2-PLpro-C111S, the cell pellet was resuspended in lysis buffer (50 mM Tris-HCl, 150 mM NaCl, 10 mM Imidazole, 1 mM TCEP, pH 7.4) and lysed by sonication and centrifuged at 13,000 rpm to clarify the supernatant. The supernatant was incubated 2 hours with TALON beads (Takara) pre-equilibrated with lysis buffer and non-specific proteins were cleared with washing. Proteins were eluted with elution buffer (50 mM Tris-HCl, 150 mM NaCl, 250 mM Imidazole, 1 mM TCEP, pH 7.4) and further purified on size-exclusion column (Superdex 75 16/60, GE Healthcare) pre-equilibrated with 20 mM Tris-HCl, 100 mM NaCl, 1 mM TCEP, pH 7.4. Proteins were concentrated to 20 mg/ml and stored for crystallization. For the expression of mISG15, BL21(DE3) E. coli competent cells (NEB) were transformed with pACE-ISG15. Bacterial colony was in 5 ml DYT medium with 0.2% (w/v) glucose and 100 µg/ml ampicillin inoculated and grown overnight at 37 °C. The preculture was 3 min at 3000 g centrifuged and resuspended in 5 ml of fresh medium. 2 L of DYT medium were mixed with 5 ml of the Pre-culture inoculated and at 37 °C until reaching a OD₆₀₀ grown from 0.6. The protein expression was induced by adding IPTG (final concentration 1 mM). The cells were grown for 20 h at 28 °C and harvested by centrifugation (10 min, 5000 g, 4 °C). 5 g of E. coli pellet (ISG15 or ISG15-C76S) were thawed on ice and in 30 ml of buffer A (ISG15) (50 mM Na₂HPO₄, 500 mM NaCl pH 7.0, 1 protease inhibitor tablet (Roche, Basel, Switzerland)) resuspended. The cells were disrupted using French pressure cell and the lysate was added for 1 h 40000 g and 4 °C centrifuged. All cleaning steps were carried out with the help of an ÄKTA chromatography system (GE Healthcare, Little Chalfont, UK) at 4 °C. The supernatant was applied to a 15 ml Ni-FF Sepharose column (GE Healthcare, Little Chalfont, UK). The column was filled with 4 column volumes of 50 mM Na₂HPO₄, 500 mM NaCl, 15 mM imidazole pH 7.0 washed and the protein with a linear imidazole gradient over 20 column volumes and final imidazole concentration

of 500 mM eluted (buffer B ISG15). About 30 mg of the eluted protein were treated with 1 mg His6-HRV-3C combined and dialyzed against buffer A (ISG15) at 16 °C for 16 h. The protein was then applied to the same column as that containing the protein Concentrated run to about 6 mg/ml and further purified with size-exclusion column (Superdex 75 16/60, GE Healthcare) pre-equilibrated with 20 mM Tris-HCl, 100 mM NaCl, 1 mM TCEP, pH 7.4.

Ubiquitin/NEDD8/SUMO-/ISG15 activity-based probes assay

PLpros were diluted (2 µM, final concentration) with activation buffer and incubated 10 minutes at 25 °C and the activity-based probes were diluted (0.2 mg/ml, final concentration) in dilution buffer (50 mM Tris-HCl 7.5, 150 mM NaCl). The reaction mixture was prepared by mixing equal volume of activated PLpros (2 µM) and activity-based probes (0.2 mg/ml). Reactions were conducted at indicated temperature (on ice or 37 °C) and samples were taken at the indicated time points and the reactions were quenched by the addition of SDS-sample buffer. Samples were further analyzed by SDS-PAGE and stained with silver staining kit (Thermo Fisher).

AMC-probes based kinetic assay

For determination of enzymatic kinetic values (k_{cat} , K_M), ubiquitin-AMC or ISG15-AMC was used as substrate of PLpro or mUSP18 and the release of AMC was measured by increase of fluorescence (Ex./Em. 360/487 nm) on 384-well microplate reader (PHERAstar FSX, BMG Labtech). 5 µl of solution containing different concentration of K48-Ub₂-AMC (76 - 0 µM) or ISG15-AMC (40 - 0 µM) were aliquoted into 384 well plate and reaction was initiated by addition of 5 µl of PLpro or mUSP18 (20 nM) to the well. Initial velocities of AMC-release were normalized to standard curve and the velocity versus substrate concentration plot were further analyzed by Michaelis-Menten enzymatic kinetics- k_{cat} function with fixed value of total enzyme concentration as provided above. The experiment was repeated at least three times.

Bio-Layer Interferometry (BLI)

Binding kinetics were determined with OctetRed system (Fortebio). 1 µM of either SCoV2-PLpro C111S or SCoV-PLpro C111S were loaded onto Ni-NTA biosensor and equilibrated with binding buffer for the baseline. To examine the association rate, equilibrated sensors were transferred into solutions containing various concentration of K48-Ub₂ (90 - 0 µM) or hISG15 (3 - 0 µM) or mISG15 (90 - 0 µM). Dissociation of PLpro was initiated by placing sensor into reaction buffer again. Association rate constant (k_{on}), dissociation rate constant (k_{off}), dissociation constant (K_d) values were calculated by Octet Data analysis software (Fortebio).

Crystallization

Equal amounts of SCoV2-PLpro -C111S and full-length murine ISG15 were mixed and the final concentration of mixture was 250 µM. Protein mixture were screened with sitting drop matrix screens in 96-well plate with 100 nl of protein and 100 nl of precipitant solution at 293K. Initial crystals appeared from solution containing 20% PEG 3350, 200 mM Potassium thiocyanate with 125 µM protein concentration. To optimize the crystallization condition, we diluted the protein to vary the concentration and the diffraction-quality crystals were grown in optimized solution containing 18% PEG 3350, 100 mM bis-tris propane pH 6.5, 200 mM Potassium thiocyanate with 100 µM protein concentration.

Data collection, processing and structure determination

Crystals were cryo-protected using mother liquor solution supplemented with 25% (v/v) ethylene glycerol. Diffraction data were collected on single frozen crystal in a nitrogen stream at 100 K at 1.00001 Å at X06SA beamline in Swiss Light Source, Villigen. Initial data sets were processed using XDS⁴², and phases were determined by Phaser molecular replacement in ccp4 module with SCoV2-PLpro, mISG15 as template model⁴³, PDB IDs: 6W9C and 5TLA, respectively). Structure

refinement and manual model building were performed with Coot and Phenix.Refine^{44,45} (Extended Data Table.1). There are 93.26% and 6.74% of the residues in the favoured/allowed regions of the Ramachandran plot respectively, and no residues are found in disallowed regions.

Cell lysates deubiquitination and deISGylation assay

HeLa or A549 cells were treated with IFN- α (200 U/ml) for 48 hrs to induce ISGylation. Cells were lysed with lysis buffer (50 mM Tris-HCl (pH 8.0), 150 mM NaCl, 1% (v/v) NP-40) and concentration was measured with BCA assay (Thermo Fischer). 10 μ g of lysates were incubated with 100 nM of PLpro for indicated timepoints at 37 °C and analyzed by immunoblotting with indicated antibodies. To test inhibitory effect of GRL-0617, 40 μ M of GRL-0617 was included during reaction. Images were obtained from Image lab software (Biorad).

Deneddylation and I κ B α deubiquitination assay

All proteins described are of human origin. CUL1-RBX1, SKP1- β -TRCP2, UBE2M, UBE2D3, NEDD8, UB, APPBP1-UBA3, UBA1 were purified as previously described⁴⁶. Neddylated CUL1-RBX1 was generated as previously described⁴⁶. Reaction for generating hyperneddylated CUL1-RBX1 was driven at pH 8.8 at 37 °C for 30 min, and purified by size exclusion chromatography. USP2 catalytic core was purified with nickel affinity chromatography, liberated of the His-tag by overnight thrombin cleavage, following IEX and size exclusion chromatography. Den1 was purified by GST affinity chromatography, liberated of the GST tag by overnight TEV cleavage, following IEX and size exclusion chromatography. The Cop9 signalosome (CSN) was purified as previously described⁴⁷. Deneddylation assays were performed with 1 μ M hyperneddylated CUL1-RBX1, and 5 μ M protease (SCoV-PLpro, SCoV2-PLpro, DEN1, USP2) or 20 nM CSN. Reaction was performed at 37 °C in 2.5mM Tris 100 mM NaCl, 5mM DTT pH 8.5, and in the case of CSN with additional 10mM MgCl₂. Samples were taken at each indicated time point and quenched with 2X SDS-PAGE sample buffer. Gels were stained by Coomassie-blue and scanned on an Amersham imager 600. I κ B α Deubiquitylation assays were performed by first generating a ubiquitylated I κ B α , with 200 nM UBA1, 1 μ M UBE2D3, 20 μ M UB, 500 nM neddylated CRL1 ^{β -TRCP}, and 5 μ M fluorescently labelled I κ B α at 37 °C in 50 mM Tris 50mM NaCl 10mM MgCl₂ 5mM DTT pH 7.5 for 30 minutes. Reaction was quenched by adding 80mM EDTA for 5 minutes. Deubiquitylation reaction was started by mixing 3 μ M of protease (SCoV-PLpro, SCoV2-PLpro, USP2) with the ubiquitylation reaction, and samples were taken at each time point and quenched with 2X SDS-PAGE sample buffer. Gels were scanned on an Amersham Typhoon (GE) detecting the fluorescently labelled I κ B α .

Molecular Dynamics Simulations

SCoV-PLpro (wild type and double mutant) and SCoV2-PLpro with K48-Ub₂. The coordinates of SCoV-PLpro with bound K48-Ub₂ were taken from PDB ID: 5E6J⁴⁸. For the double mutant set up, the mutations S67V and L76T were introduced using MODELLER⁴⁹. For SCoV2-PLpro with bound K48-Ub₂, we set up two models. We combined the substrate coordinates taken from PDB ID: 5E6J with 1) the X-ray crystal structure of the unbound form (PDB ID: 6W9C, re-refined by Tristan Croll (<https://drive.google.com/drive/folders/1JBo50CdkBU7K1pFThuqrzqH-NcslAWyG>) and 2) with the X-ray crystal structure SCoV2-PLpro:mISG15 (PDB ID: 6YVA) after PLpro alignment using PyMol⁵⁰. In all di-ubiquitin systems the triazole linker was replaced with Lys using MODELLER. To mimic the linker, a harmonic distance restraint potential was applied between the backbone carbonyl carbon atoms of Lys48 and Gly75 with a target distance of 9.5 Å and a force constant of 502080 kJ mol⁻¹ nm⁻². The covalent propargylamide linker was removed.

SCoV-PLpro and SCoV2-PLpro in complex with inhibitor GRL-0617. The coordinates of the SCoV-PLpro:GRL-0617 complex were taken from PDB ID: 3E9S¹⁷. The oxidized Cys112 was changed to the reduced form (SH) using MODELLER. The simulation model of the

SCoV2-PLpro:GRL-0617 complex was built according to the X-ray structure of the unbound form of SCoV2-PLpro (PDB ID: 6W9C, re-refined by Tristan Croll). The coordinates of the compound GRL-0617 were modeled according to PDB ID: 3E9S after PLpro alignment using PyMol. The blocking loop 2 (BL2 loop, GNYQCGH) capping the GRL-0617 binding site was remodeled according to the SCoV-PLpro X-ray crystal structure of the complex (PDB ID: 3E9S)¹⁷ using MODELLER. The GRL-0617 ligand was parameterized with the General Amber Force Field (GAFF)⁵¹.

SCoV2-PLpro with mISG15. The X-ray crystal structure SCoV2-PLpro:mISG15 (PDB ID: 6YVA) served as starting point. Missing residues of SCoV2-PLpro and one Zn ion were modeled according to the X-ray crystal structure (PDB ID: 6W9C, re-refined by Tristan Croll).

Missing side chains in all setups were modeled using MODELLER. All crystallographic water molecules and ions were retained, except a nickel ion in PDB ID: 5E6J. According to pKa calculations using PropKa and additional visual inspections, in all setups His17 of SCoV2-PLpro (His18 of SCoV-PLpro) and His272 of SCoV2-PLpro (His273 of SCoV-PLpro) were charged. We cannot exclude that the protonation state of the catalytic His272 of SCoV2-PLpro (His273 of SCoV-PLpro) is in equilibrium between charged and neutral forms. All other residues were simulated in their physiological protonation state. The proteins were solvated in TIP4P-D water⁵² with 150 mM NaCl. MD simulations were carried out using Gromacs 2018⁵³ and the AMBER99SB*-ILDN-q force field⁵⁴⁻⁵⁷. Each system was energy minimized, followed by five equilibration steps, in which we gradually weakened the position restraints on heavy atoms, first in an NVT ensemble (0.25 ns) and then in an NPT ensemble (4 x 0.5 ns) using a Berendsen thermostat and barostat⁵⁸. Production simulations were run at a temperature of 310 K and a pressure of 1 bar in an NPT ensemble using a Nosé-Hoover thermostat^{59,60} and a Parrinello-Rahman barostat⁶¹. We set up three independent runs of the SCoV2-PLpro systems with bound substrates, starting from different MODELLER results for the apo-like model of SCoV2-PLpro:K48-Ub₂ and for SCoV2-PLpro:mISG15. For simulations with bound substrates and with bound inhibitor, we monitored the root-mean-square deviation (RMSD) of each backbone substrate (distal ubiquitin in K48-Ub₂ and N-terminal domain of mISG15) and of GRL-0617 (heavy atoms) to the respective equilibrated structure after alignment on the helix backbone of PLpro (without the flexible UBL domain). From simulations of SCoV-PLpro:K48-Ub₂, we extracted the minimum heavy-atom distance between F70 of SARS and I44 of ubiquitin.

Inhibitor IC₅₀ determination

For IC₅₀ value for inhibitors, ubiquitin-AMC or ISG15-AMC was used as substrate of PLpro and the release of AMC was measured by increase of fluorescence (Ex./Em. 360/487 nm) on 384-well microplate reader (PHERAstar FSX, BMG Labtech). 5 μ l of solution containing different concentration of GRL-0617 (200 – 0 μ M) and 10 μ M of ubiquitin-/ISG15-AMC were aliquoted into 384 well plate and reaction was initiated by addition of 5 μ l of PLpro (30 nM) to the well. Initial velocities of AMC-release were normalized against to DMSO control. IC₅₀ value is calculated by Dose-response – Inhibition function in Graphpad Prism with [inhibitor] vs normalized response equation. The experiment was repeated three times.

Mass-spectrometry

For interactome analysis, A549 cells were transfected with SCoV-PLpro or SCoV2-PLpro wt or mutant (C111S) and for comparison between SARS and SARS-CoV-2, mutant PLpro (C111S) versions for both proteins were transfected. Cells were stimulated with Interferon- α (200 units/ml) for 36 hours to mimic infection scenario. Cells were lysed in ice cold lysis buffer (50 mM Tris-Cl, pH 7.5; 150 mM NaCl; 1% Triton x-100) and equal amounts of lysates were incubated with GFP nanotrapp beads in IP buffer (Lysis buffer without detergent). After incubation, IPs were washed three times with wash buffer (50 mM Tris-HCl, pH7.5; 400 mM

Article

NaCl; 0.5 mM EDTA) and two times with IP buffer. Then beads were incubated with 25 μ l of 50 mM Tris-HCl (pH 8.5) containing 4 M urea, 1 mM TCEP, 4 mM Chloroacetamide for 1 hour in the dark at 37 °C. Afterwards, samples were then diluted with 50 mM Tris-HCl pH 8.5 to final urea conc. < 2M and digested with 0.5 μ g Trypsin (Promega) at 37 °C overnight. Digests were acidified using trifluoroacetic acid (TFA) to a pH of 2-3 and peptides were desalted using C18-stage tips⁶². Peptides were labelled with TMT reagents (Thermo fisher) as described previously⁶³. Briefly, peptides were resuspended in TMT labelling buffer (0.2 M EPPS pH 8.2, 20% Acetonitrile) and were mixed with TMT reagents in a 2:1 TMT : peptide ratio. Reaction was performed for one hour at RT and subsequently quenched by addition of hydroxylamine to a final concentration of 0.5% at RT for 15min. Samples were pooled in equimolar ratio, acidified, and again cleaned-up using C18-stage tips. After drying, peptides were resuspended in 0.1% formic acid (FA) for LC-MS. All mass spectrometry data was acquired in centroid mode on an Orbitrap Fusion Lumos mass spectrometer hyphenated to an easy-nLC 1200 nano HPLC system with a nanoFlex ion source (ThermoFisher Scientific). A spray voltage of 2.6 kV was applied with the transfer tube heated to 300 °C and funnel RF set to 30%. Internal mass calibration was enabled (lock mass 445.12003 m/z). Peptides were separated on a self-made 32 cm long, 75 μ m ID fused-silica column, packed in house with 1.9 μ m C18 particles (ReproSil-Pur, Dr. Maisch) and heated to 50 °C using an integrated column oven (Sonation). HPLC solvents consisted of 0.1% Formic acid in water (Buffer A) and 0.1% Formic acid, 80% acetonitrile in water (Buffer B). Peptides were eluted by a non-linear gradient from 7 to 40% B over 90 minutes followed by a step-wise increase to 95% B in 6 minutes which was held for another 9 minutes. Full scan MS spectra (350-1400 m/z) were acquired with a resolution of 120,000 at m/z 200, maximum injection time of 100 ms and AGC target value of 4×10^5 . The 20 most intense precursors per full scan with a charge state between 2 and 5 were selected for fragmentation ("Top 20"), isolated with a quadrupole isolation window of 0.7 Th and fragmented via HCD applying an NCE of 38%. MS2 scans were performed in the Orbitrap using a resolution of 50,000 at m/z 200, maximum injection time of 86ms and AGC target value of 1×10^5 . Repeated sequencing of already acquired precursors was limited by setting a dynamic exclusion of 60 seconds and 7 ppm and advanced peak determination was deactivated. MS raw data was analyzed with Proteome Discoverer (PD, version 2.4, ThermoFisher Scientific) using Sequest HT as a search engine and performing re-calibration of precursor masses by the Spectrum RC-node. Fragment spectra were searched against the human reference proteome ("one sequence per Gene", 20531 sequences, version March 2020) and protein sequences for SARS (15 sequences, version March 2020) and CoV2 (14 sequences, version February 2020) downloaded from Uniprot in March 2020 as well as common contaminants as included in "contaminants.fasta" provided with the MaxQuant software. Static modifications were TMT at the peptide N-terminus and lysines as well as carbamidomethyl at cysteine residues, dynamic modifications were set as Oxidation of Methionine and Acetylation at the protein-N-term. Matched spectra were filtered with Percolator applying a false discovery rate of 1% on PSM and protein level. Reporter intensities were normalized to the total protein intensities in PD assuming equal sample loading and additionally by median-normalization using the NormalizerDE package⁶⁴. Statistically significant changes between samples were determined in Perseus (version 1.6.6.0) and significant candidates were chosen having *p*-value ≤ 0.01 and Log2 fold change value minimum ± 0.5 ⁶⁵.

Cell culture

Human CaCo-2 cells were obtained from the Deutsche Sammlung von Mikroorganismen und Zellkulturen (DSMZ; Braunschweig, Germany). Cells were grown at 37 °C in Minimal Essential Medium (MEM) supplemented with 10% fetal bovine serum (FBS) and containing 100 IU/ml penicillin and 100 μ g/ml streptomycin. A549 and HeLa cells were obtained from ATCC (ATCC CCL-185, ATCC CCL-2, respectively). All the cell lines used tested negative for mycoplasma.

Antibodies

We have used following antibodies and dilutions for this study. Ubiquitin (Cat# 3936S, Provider: Cell signaling Technology, 1:2000), ISG15 (Cat# HPA004627, Sigma Aldrich/Merck, 1:1000), GAPDH (Cat# 2118, Cell signaling Technology, 1:2000), GFP trap beads (Cat #: gta-100, Provider: ChromoTek), GFP (Cat# sc-9996, Santa Cruz Biotechnology, 1:2000), IRF3 (Cat# 4302, Cell signaling Technology, 1:2000), phospho-IRF3(Ser396) (Cat# 4947, Cell signaling Technology, 1:1000), I κ B α (Cat# 4812, Cell signaling Technology, 1:2000), phospho-I κ B α (Ser32/36) (Cat# 9246, Cell signaling Technology, 1:1000), TBK1 (Cat# 3013, Cell signaling Technology, 1:2000), pTBK1 (Cat # 3300-1 Epitomics, 1:1000), P65 (NF κ B) (Cat# 8008, Santa Cruz Biotechnology, 1:2000), Lamin B1 (Cat# sc-373918, Santa Cruz Biotechnology, 1:2000).

Virus preparation

SARS-CoV-2/FFM1 (Accession: MT358638)⁶⁶ was isolated from travellers returning from Wuhan (China) to Frankfurt (Germany) using CaCo-2 cells. SARS-CoV-2/FFM1 stocks used in the experiments had undergone one passage on CaCo-2 cells as described previously²⁴. Virus titers were determined as TCID₅₀/ml in confluent cells in 96-well microtiter plates.

Antiviral and cytotoxicity assays

Confluent layers of CaCo-2 cells in 96-well plates were infected with SARS-CoV-2/FFM1 at MOI 0.01. Virus was added simultaneously with GRL-0617 and incubated in MEM supplemented with 1% FBS with different drug dilutions. Cytopathogenic effect (CPE) was assessed visually 48 h after infection. To assess effects of GRL-0617 on CaCo-2 cell viability, confluent cell layers were treated with different drug concentration. Cell viability was determined by 3-(4,5-dimethylthiazol-2-yl)-2,5-diphenyltetrazolium bromide (MTT) assay modified after Mosman⁶⁷, as previously described⁶⁸. Data for each condition was collected for at least three biological replicates.

Luciferase activity assay

To analyze the induction of IFN β induced genes, a luciferase reporter assay was used in A549 cells. Briefly, an expression construct containing the luciferase ORF and the IFN β promoter (IFN β /luciferase) was co-transfected with either a GFP control plasmid or the designated PLpro plasmid. For all transfections, 100 ng of luciferase plasmid, 400ng of PLpro or GFP vector was used in each well of a 12 well plate. All transfections were performed in triplicate and the average of 3 experiments is shown in figures. 24h post transfection cells were treated with 500ng poly I:C for 18h or 50ng/ml of TNF α for 30min. Luciferase expression was measured Luciferase Reporter assay system (Promega Inc). Fold change is calculated by taking vector treated with poly I:C or TNF- α as 1.

Immunofluorescence and confocal imaging

HeLa cells expressing GFP tagged PLpro was treated with TNF α (50ng/ml) for 45min. Cells were fixed with paraformaldehyde, blocked in 5% serum and immunostained overnight at 4 °C with antibody against p65. Confocal imaging was performed using the Zeiss LSM780 microscope system. An Ar-ion laser (for excitation of GFP at 488 nm), a He-Ne laser (for excitation Alexa Fluor 546nm) were used with a 63 \times 1.4 NA oil immersion objective. Images were analysed in Fiji to check for colocalization between DAPI and immunostained p65. Results are indicative of 50 cells taken from 3 independent experiments; error bars indicate standard deviation.

Nuclear Fractionation

A549 cells from a confluent 60 mm dish were transiently transfected with GFP tagged PLPro followed by treatment with interferon α (200u/ml, 36h). Cells were lysed in hypotonic buffer [10 mmol/L HEPES (pH = 7.4), 2 mmol/L MgCl₂, 25 mmol/L KCl, 1 mmol/L DTT, 1 mM PMSF, and protease

inhibitor cocktail], kept on ice for 30 min followed by syringe lysis, 2 mol/L sucrose solution was added dropwise, followed by centrifugation at 1000g for 15 min. The supernatant was saved as the cytosolic fraction. The pellet was washed twice in wash buffer [10 mmol/L HEPES (pH = 7.4), 2 mmol/L MgCl₂, 25 mmol/L KCl, 250 mmol/L sucrose, 1 mmol/L DTT, 1 mmol/L PMSF, and protease inhibitor cocktail] and saved as the nuclear fraction.

Quantification of viral and cellular RNA

SARS-CoV-2 RNA from cell culture supernatant samples was isolated using ACL buffer and the QIAamp 96 Virus kit (Qiagen) according to the manufacturer's instructions. RNA was subjected to OneStep qRT-PCR analysis using the LightCycler Multiplex RNA Virus Master kit (Roche). Intracellular RNA was isolated using RLT buffer and the RNeasy 96 HT Kit according to the manufacturer's instructions. PCR was performed on a CFX96 Real-Time System, C1000 Touch Thermal Cycler. Primers and probe were adapted from the WHO protocol⁶⁹ targeting the open reading frame for RNA-dependent RNA polymerase (RdRP) of both SARS-CoV-2: RdRP_SARSr-F2 (GTGARATGGTCATGTGTGGCGG) and RdRP_SARSr-R1 (CARATGTTAAASACACTATTAGCATA) primers were used in a final concentration of 0.4 μM and RdRP_SARSr_P2 probe (6-Fam CAGGTGGAACCTCATCAGGAGATGC BBQ1) was used with 0.2 μM, respectively. Primers for ACTB (fwd: CATCGAGCACGGC ATCGTCA; rev: TAGCACAGCTGGATAGCAAC)⁷⁰, ISG15 (fwd: GAGAGGCA GCGAACTCATCT; rev: AGGGACACCTGGAATTCGTT)⁷¹ IL6 (fwd: GCAGAA AAGGCAAAGAATC; rev: CTACATTTGCCGAAGAGC), IL8 (fwd: GTTT TTGAAGAGGGCTGAG; rev: TTTGCTTGAAGTTTCACTGG), and 18S rRNA (fwd: AGAAACGGCTACCACATCCA; rev: CACCAGACTTGCCCTC CA) were used for SYBR green based detection of cellular genes in a final concentration of 0.4 μM per reaction. For each condition, three biological replicates were used. Mean and standard deviation were calculated for each group. For interferon responsive genes, following primers were used. MX1 (fwd: TTTTCAAGAAGGAGGCCAGCAA; rev: TCAGAACTTCCGTTGTGTCG), OAS1 (fwd: TGGCCTTATGCCCTCTAT CC; rev: TCCCATCAGGTGCACAGAAGA) and PKR (fwd: GGAACCTTGGCAT ACATGAGCC; rev: GTCGCCGTAGGTCAAGTGAAGAAA). SARS-CoV-2 subgenomic RNA4 encoding E gene, which is processed during discontinuous transcription in productively infected cells⁷² was quantified using primer pairs (fwd: AACGTACCTGTCTCTCCGA; rev: CCAACCAA CTTTCGATCTCTTGT) spanning a junction of the SARS-CoV-2 subgenomic RNAs and used as a measure of active viral.

Reporting summary

Further information on research design is available in the Nature Research Reporting Summary linked to this paper.

Data and code availability

The atomic coordinates of PLpro-ISG15 (murine) have been deposited in the PDB with accession code 6YVA in the Protein Data Bank. The mass spectrometry proteomics data have been deposited to the ProteomeXchange Consortium⁷³ via the PRIDE partner repository⁷⁴ with the dataset identifier PXD018983. The papain-like protease domain sequence is obtained from SARS-CoV-2 complete genome (NCBI genome databank, Severe acute respiratory syndrome coronavirus 2 isolate Wuhan-Hu-1, complete genome; NC_045512). Protein sequence for CoV2 PLpro-Ubl domain (amino acids, 746-1060) of Nsp3 protein from SARS-CoV-2 (Nsp3; YP_009725299.1). Full gel images can be found in Supplementary Figure 1 and source data that support this study and can be found in Supplementary Information. Any other relevant data are available from the corresponding authors upon reasonable request. Source data are provided with this paper.

1. Daczkowski, C. M., Goodwin, O. Y., Dzimiński, J. V., Farhat, J. J. & Pegan, S. D. Structurally Guided Removal of DelSGylase Biochemical Activity from Papain-Like Protease Originating from Middle East Respiratory Syndrome Coronavirus. *J. Virol.* **91**, (2017).
2. Kabsch, W. XDS. *Acta Crystallogr. Sect. D Biol. Crystallogr.* **66**, 125–132 (2010).

3. McCoy, A. J. et al. Phaser crystallographic software. *J. Appl. Crystallogr.* **40**, 658–674 (2007).
4. Afonine, P. V. et al. Towards automated crystallographic structure refinement with phenix.refine. *Acta Crystallogr. Sect. D Biol. Crystallogr.* **68**, 352–367 (2012).
5. Emsley, P., Lohkamp, B., Scott, W. G. & Cowtan, K. Features and development of Coot. *Acta Crystallogr. Sect. D Biol. Crystallogr.* **66**, 486–501 (2010).
6. Baek, K. et al. NEDD8 nucleates a multivalent cullin-RING-UBE2D ubiquitin ligation assembly. *Nature* **578**, 461–466 (2020).
7. Enchev, R. I. et al. Structural Basis for a Reciprocal Regulation between SCF and CSN. *Cell Rep.* **2**, 616–627 (2012).
8. Békés, M. et al. Recognition of Lys48-Linked Di-ubiquitin and Deubiquitinating Activities of the SARS Coronavirus Papain-like Protease. *Mol. Cell* **62**, 572–585 (2016).
9. Šali, A. & Blundell, T. L. Comparative Protein Modelling by Satisfaction of Spatial Restraints. *J. Mol. Biol.* **234**, 779–815 (1993).
10. Schrödinger, L. The PyMol Molecular Graphics System, Version 1.8. *Thomas Holder* (2015) <https://doi.org/10.1007/s13398-014-0173-72>.
11. Wang, J., Wolf, R. M., Caldwell, J. W., Kollman, P. A. & Case, D. A. Development and testing of a general amber force field. *J. Comput. Chem.* **25**, 1157–1174 (2004).
12. Piana, S., Donchev, A. G., Robustelli, P. & Shaw, D. E. Water Dispersion Interactions Strongly Influence Simulated Structural Properties of Disordered Protein States. *J. Phys. Chem. B* **119**, 5113–5123 (2015).
13. Abraham, M. J. et al. GROMACS: High performance molecular simulations through multi-level parallelism from laptops to supercomputers. *SoftwareX* **1–2**, 19–25 (2015).
14. Hornak, V. et al. Comparison of multiple Amber force fields and development of improved protein backbone parameters. *Proteins Struct. Funct. Bioinforma.* **65**, 712–725 (2006).
15. Best, R. B., de Sancho, D. & Mittal, J. Residue-Specific α -Helix Propensities from Molecular Simulation. *Biophys. J.* **102**, 1462–1467 (2012).
16. Best, R. B. & Hummer, G. Optimized Molecular Dynamics Force Fields Applied to the Helix-Coil Transition of Polypeptides. *J. Phys. Chem. B* **113**, 9004–9015 (2009).
17. Lindorff-Larsen, K. et al. Improved side-chain torsion potentials for the Amber ff99SB protein force field. *Proteins Struct. Funct. Bioinforma.* NA-NA (2010) <https://doi.org/10.1002/prot.22711>.
18. Berendsen, H. J. C., Postma, J. P. M., van Gunsteren, W. F., DiNola, A. & Haak, J. R. Molecular dynamics with coupling to an external bath. *J. Chem. Phys.* **81**, 3684–3690 (1984).
19. Evans, D. J. & Holian, B. L. The Nose-Hoover thermostat. *J. Chem. Phys.* **83**, 4069–4074 (1985).
20. Nosé, S. A unified formulation of the constant temperature molecular dynamics methods. *J. Chem. Phys.* **81**, 511–519 (1984).
21. Parrinello, M. & Rahman, A. Polymorphic transitions in single crystals: A new molecular dynamics method. *J. Appl. Phys.* **52**, 7182–7190 (1981).
22. Rappsilber, J., Ishihama, Y. & Mann, M. Stop and Go Extraction Tips for Matrix-Assisted Laser Desorption/Ionization, Nano-electrospray, and LC/MS Sample Pretreatment in Proteomics. *Anal. Chem.* **75**, 663–670 (2003).
23. Klann, K., Tascher, G. & Münch, C. Functional Translome Proteomics Reveal Converging and Dose-Dependent Regulation by mTORC1 and eIF2 α . *Mol. Cell* **77**, 913–925.e4 (2020).
24. Willforss, J., Chawade, A. & Levander, F. NormalizerDE: Online Tool for Improved Normalization of Omics Expression Data and High-Sensitivity Differential Expression Analysis. *J. Proteome Res.* **18**, 732–740 (2019).
25. Tyanova, S. et al. The Perseus computational platform for comprehensive analysis of (pro)teomics data. *Nat. Methods* **13**, 731–740 (2016).
26. Toptan, T. et al. Optimized qRT-PCR approach for the detection of intra- and extracellular SARS-CoV-2 RNAs. *bioRxiv* (2020) <https://doi.org/10.1101/2020.04.20.052258>.
27. Mosmann, T. Rapid colorimetric assay for cellular growth and survival: Application to proliferation and cytotoxicity assays. *J. Immunol. Methods* **65**, 55–63 (1983).
28. Onafuye, H. et al. Doxorubicin-loaded human serum albumin nanoparticles overcome transporter-mediated drug resistance in drug-adapted cancer cells. *Beilstein J. Nanotechnol.* **10**, 1707–1715 (2019).
29. Corman, V. M. et al. Detection of 2019 novel coronavirus (2019-nCoV) by real-time RT-PCR. *Eurosurveillance* **25**, (2020).
30. Zhang, X., Ding, L. & Sandford, A. J. Selection of reference genes for gene expression studies in human neutrophils by real-time PCR. *BMC Mol. Biol.* **6**, (2005).
31. Moll, H. P., Maier, T., Zommer, A., Lavoie, T. & Brostjan, C. The differential activity of interferon- α subtypes is consistent among distinct target genes and cell types. *Cytokine* **53**, 52–59 (2011).
32. Kim, D. et al. The Architecture of SARS-CoV-2 Transcriptome. *Cell* **181**, 914–921.e10 (2020).
33. Vizcaino, J. A. et al. ProteomeXchange provides globally coordinated proteomics data submission and dissemination. *Nat. Biotechnol.* **32**, 223–226 (2014).
34. Vizcaino, J. A. et al. 2016 update of the PRIDE database and its related tools. *Nucleic Acids Res.* **44**, D447–D456 (2016).

Acknowledgements We thank Andrea Gubas, Claudio Joazeiro, Daniela Hoeller and Kerstin Koch for critical comments on the manuscript. We also thank Swiss Light Source (SLS) for providing special beamtime for this project during the peak of the Covid-19 pandemic in Switzerland and Wang Meitian and Olieric Vincent for providing on-site support during the data collection. This work was supported by the DFG-funded Collaborative Research Centre on Selective Autophagy (SFB 1177), by the Max Planck Society, by NWO (H.O. and G.J.v.d.H.v.N.) by the European Research Council (ERC) under the European Union's Horizon 2020 research and innovation programme (grant agreement No 789016) to BAS, LYSFOR2625 (DFG) to AB and (grant agreement No 742720) to I.D., by the grants from Else Kroener Fresenius Stiftung, Dr. Rolf M. Schwiete Stiftung, and by internal IBC2 funds to I.D.

Author contributions DS and ID conceived the project. DS contributed protein purification, biochemical and biophysical activity assay and structure determination. RM performed cell biology experiments. DG contributed protein purification. DB contributed virus infection experiments, MW and AW performed qRT-PCR measurements, KB performed denuddylation

Article

assay. AB and GT designed, performed mass spectrometry experiments and analyzed data. LS and ARM performed MD simulations. KR contributed to qRT-PCR materials and critical advice. PPG and GvdHvN synthesized Ub(l) probes and reagents in the lab of HO. SM and KPK provided Ub(l) probes and reagents. BS, GH, JC, SC and ID supervised the project. DS and ID analyzed the data and wrote the manuscript with input from all the co-authors.

Competing interests The authors declare no competing interests.

Additional information

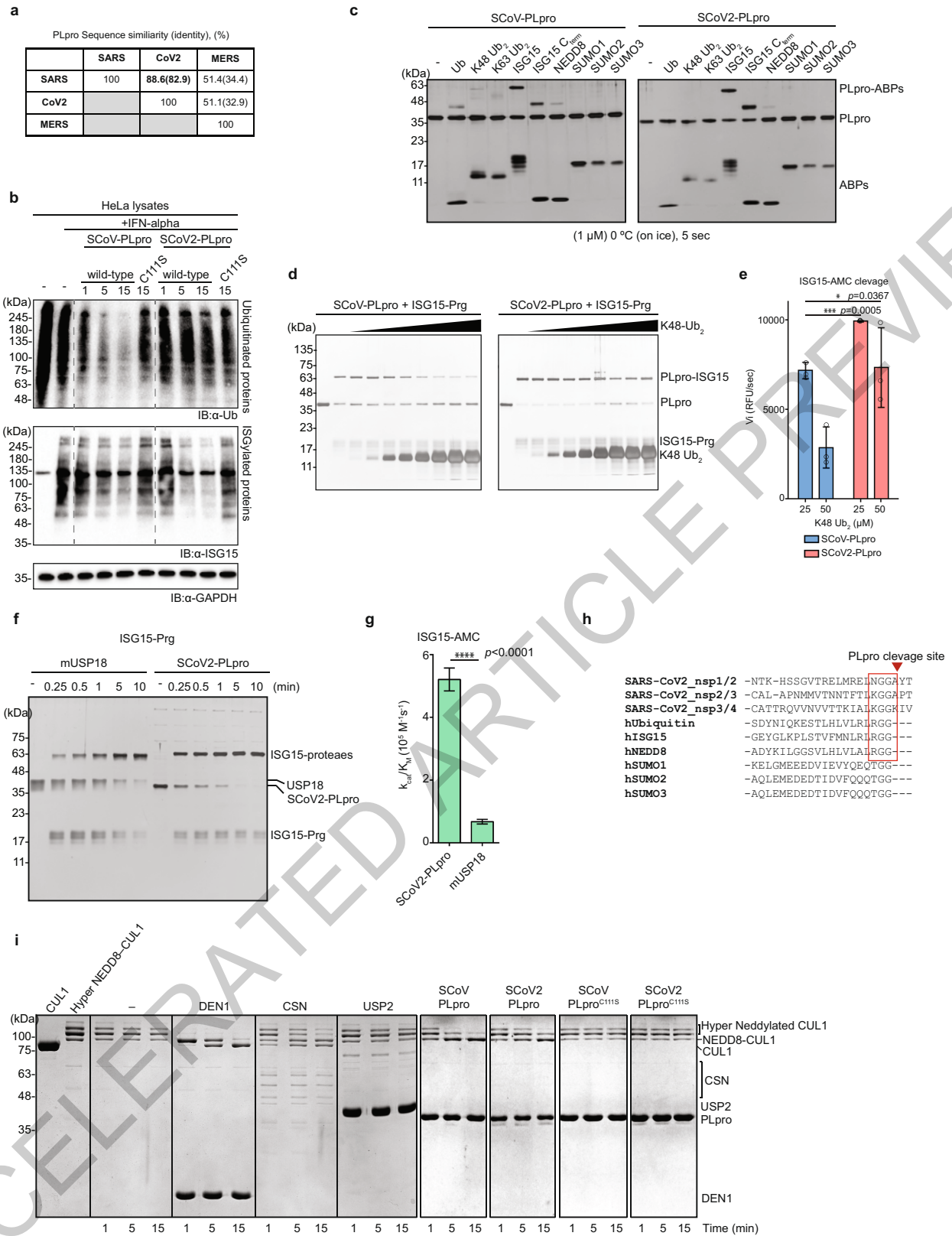
Supplementary information is available for this paper at <https://doi.org/10.1038/s41586-020-2601-5>.

Correspondence and requests for materials should be addressed to I.D.

Peer review information *Nature* thanks Rolf Hilgenfeld, Ingrid Wertz and the other, anonymous, reviewer(s) for their contribution to the peer review of this work.

Reprints and permissions information is available at <http://www.nature.com/reprints>.

ACCELERATED ARTICLE PREVIEW



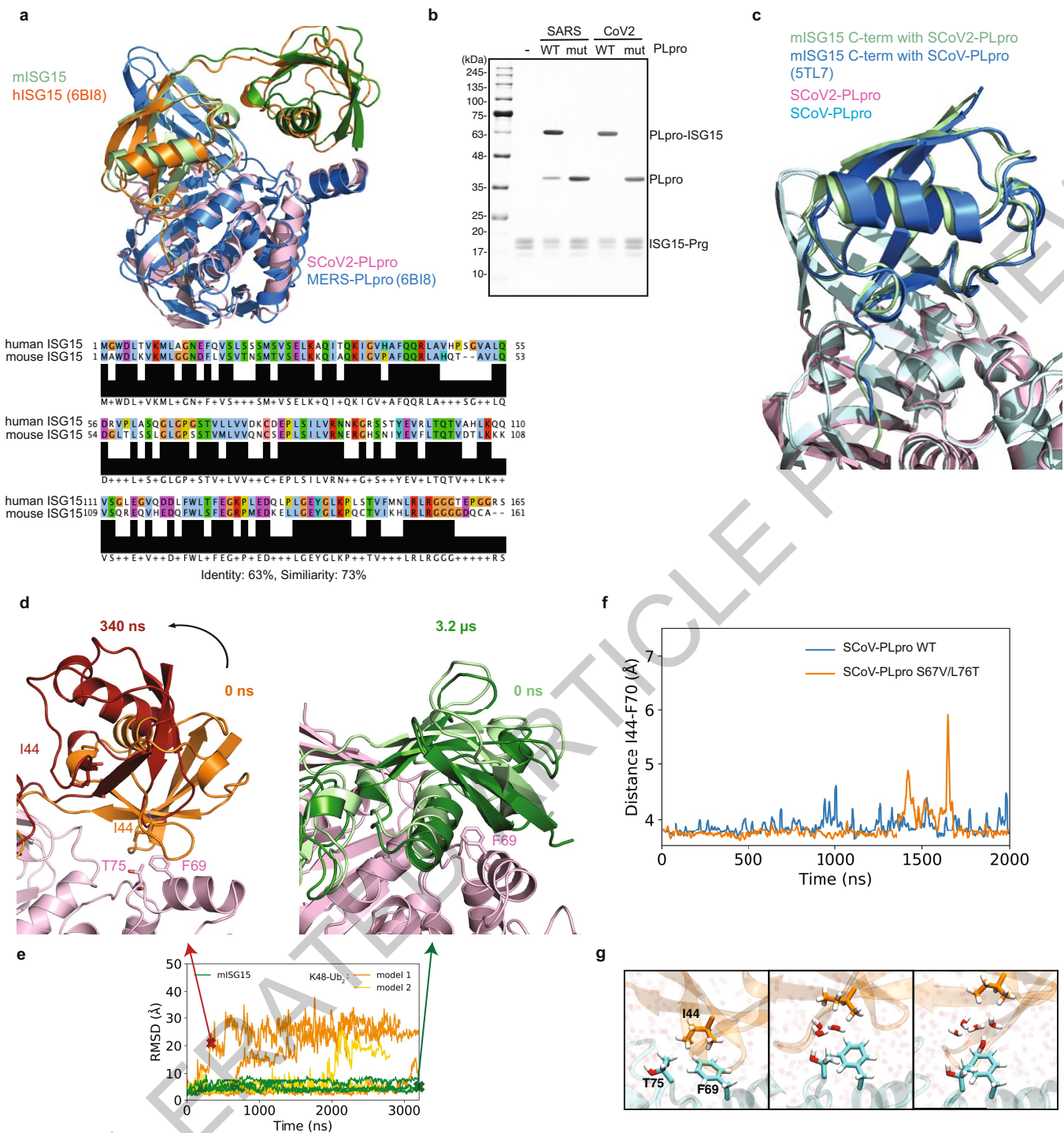
Extended Data Fig. 1 | See next page for caption.

Article

Extended Data Fig. 1 | Biochemical properties of SCoV2-PLpro. **a**, Sequence similarity of PLpro from SARS, MERS and SARS-CoV-2. **b**, IFN- α treated HeLa cell lysates were incubated with PLpro for indicated time points and analyzed by immunoblot **c**, Propargylamide-activity based probes of ubiquitin like modifiers were reacted with (left) SCoV-PLpro (right) PLpro^{CoV2}. **d**, ISG15-Prg were incubated with SCoV-PLpro (left) or SCoV2-PLpro (right) with increasing amount of non-hydrolysable K48-Ub₂. **e**, Initial AMC release rate from ISG15-AMC. Purified SCoV-PLpro and SCoV2-PLpro were incubated with ISG15-AMC and indicated amounts of K48-Ub₂. The release of AMC was measured by increase of fluorescence at (Ex./Em. 360/487 nm). **f**, Purified mUSP18 (left) and SCoV2-PLpro (right) were incubated with ISG15-propargylamide activity-based

probes for indicated time points. **g**, Catalytic efficiency (k_{cat}/K_M) of mUSP18 and SCoV2-PLpro on ISG15-AMC cleavage. **h**, Sequence alignment of PLpro cleavage site of Nsp1/2, Nsp2/3, Nsp3/4 from SARS-CoV2 and human ubiquitin like modifiers. **i**, Hyper-NEDDylated CUL1-RBX1 was incubated with purified PLpro proteins for indicated time points at 37 °C. Reactions were performed side-by-side by with well-characterized deneddylating enzymes (DEN1 with broad specificity or COP9 Signalosome CSN specific for NEDD8 linked directly to a cullin), or the broad specificity deubiquitinating enzyme USP2 as controls. Data in **e**, **g** are presented as mean \pm S.D (n=3, independent experiments). ** $p < 0.01$, *** $p < 0.001$, **** $p < 0.0001$; two-tailed paired t-tests. Experiments in **b-d**, **f**, **i** were repeated three times independently with similar results.

ACCELERATED ARTICLE PREVIEW



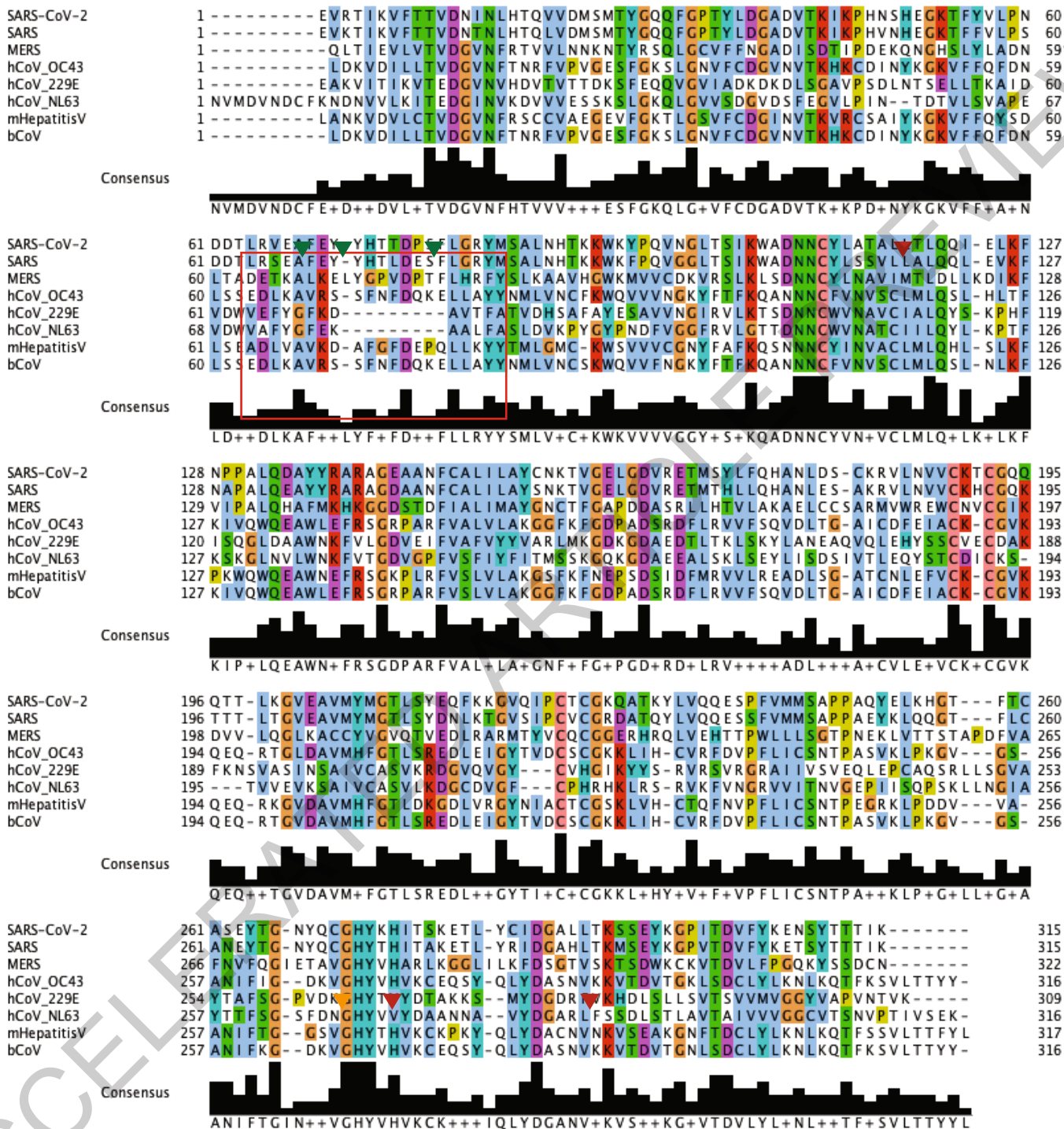
Extended Data Fig. 2 | Complex structure of SCoV2-PLpro with mouse ISG15.

a, Structural comparison of mouse ISG15:SCoV2-PLpro with human ISG15:MERS-PLpro (PDB: 6B18¹⁵) and sequence alignment of human and mouse ISG15. **b**, Activity test of wild type or catalytically inactive mutant (C111S) of SCoV-PLpro and SCoV2-PLpro. ISG15 Propargyl-activity based probes were mixed with indicated PLpro proteins. Experiments were repeated three times independently with similar results. **c**, Structural comparison of C-terminal domain of ISG15 in complex with SCoV2-PLpro and SCoV-PLpro (PDB: 5TL7¹⁶). **d**, Snapshots from molecular dynamics simulations of SCoV2-PLpro (light pink cartoon) with (left) K48-Ub₂ at 340 ns and (right) mISG15 at 3.2 μs. Key residues in the interface are highlighted. **e**, Backbone RMSD of the N-terminal domain of mISG15 (green) and of the distal ubiquitin in K48-Ub₂ in an apo-like model

(orange, model 1, SCoV2-PLpro coordinates from substrate unbound form, PDB: 6W9C) and in an mISG15-like model (yellow, model 2, SCoV2-PLpro coordinates from substrate bound form, PDB: 6YVA) from their respective SCoV2-PLpro-bound starting structures as function of time. The RMSD was calculated after superimposing the helix backbone atoms of SCoV2-PLpro. Time points for structural snapshots in **e**) are marked with a cross. **f**, Minimum heavy atom distance between F70 (SARS) and I44 (Ub) in wild type and double mutant (S67V/L76T) of SCoV-PLpro:k48-Ub₂ as function of time. **g**, Water mediated dissociation pathway. (left) Initial hydrophobic interactions between F69(CoV2), T75(CoV2) and I44(Ub). (middle) Water wedges in between T75(CoV2) and I44(Ub). (right) Water penetration between T75(CoV2)/F69(CoV2) and I44(Ub) leads to dissociation.

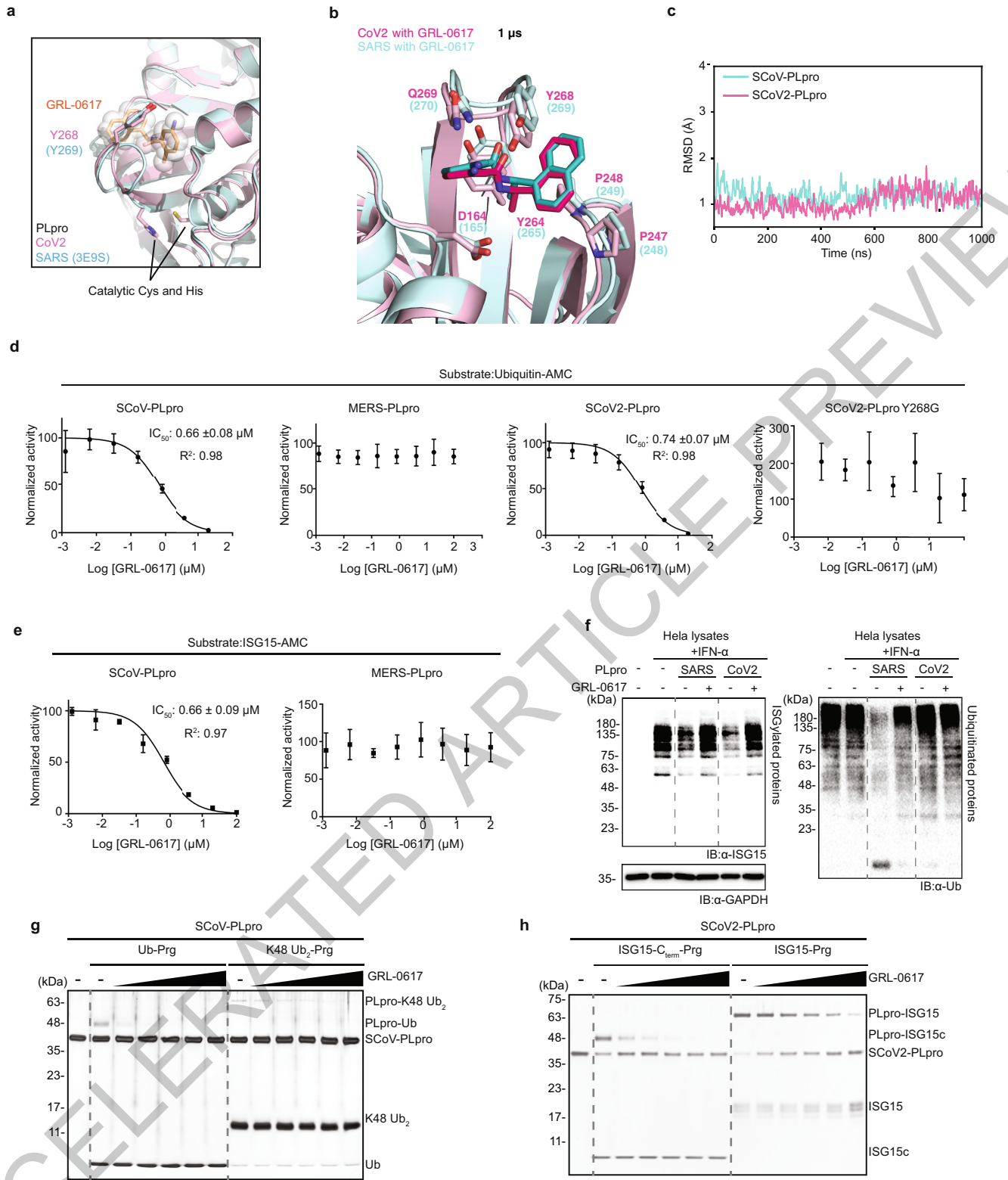
a

- S2-binding sites
- ▼ Catalytic triad
- ▼ Key residues on S2-binding sites
- ▼ GRL-0617 binding site



Extended Data Fig. 3 | Sequence alignment of papain like protease domain from corona viruses. The amino acid sequences of papain-like protease domain from eight different coronaviruses (SARS-CoV-2, SARS, MERS, humanCoV-OC43, humanCoV-229E, humanCoV-NL63, murine HepatitisV, bovine CoV) were aligned with Clustal Omega. Accession numbers: SARS-CoV-2 (NC_045512), SARS (PDB: 3MJ5), MERS (PDB: 5W8U), hCoV-OC43 (AY585228), hCoV-229E (X69721), hCoV-NL63 (NC_005831), murine HepatitisV (NC_001846), bCoV (NC_003045).

bovine CoV) were aligned with Clustal Omega. Accession numbers: SARS-CoV-2 (NC_045512), SARS (PDB: 3MJ5), MERS (PDB: 5W8U), hCoV-OC43 (AY585228), hCoV-229E (X69721), hCoV-NL63 (NC_005831), murine HepatitisV (NC_001846), bCoV (NC_003045).



Extended Data Fig. 4 | See next page for caption.

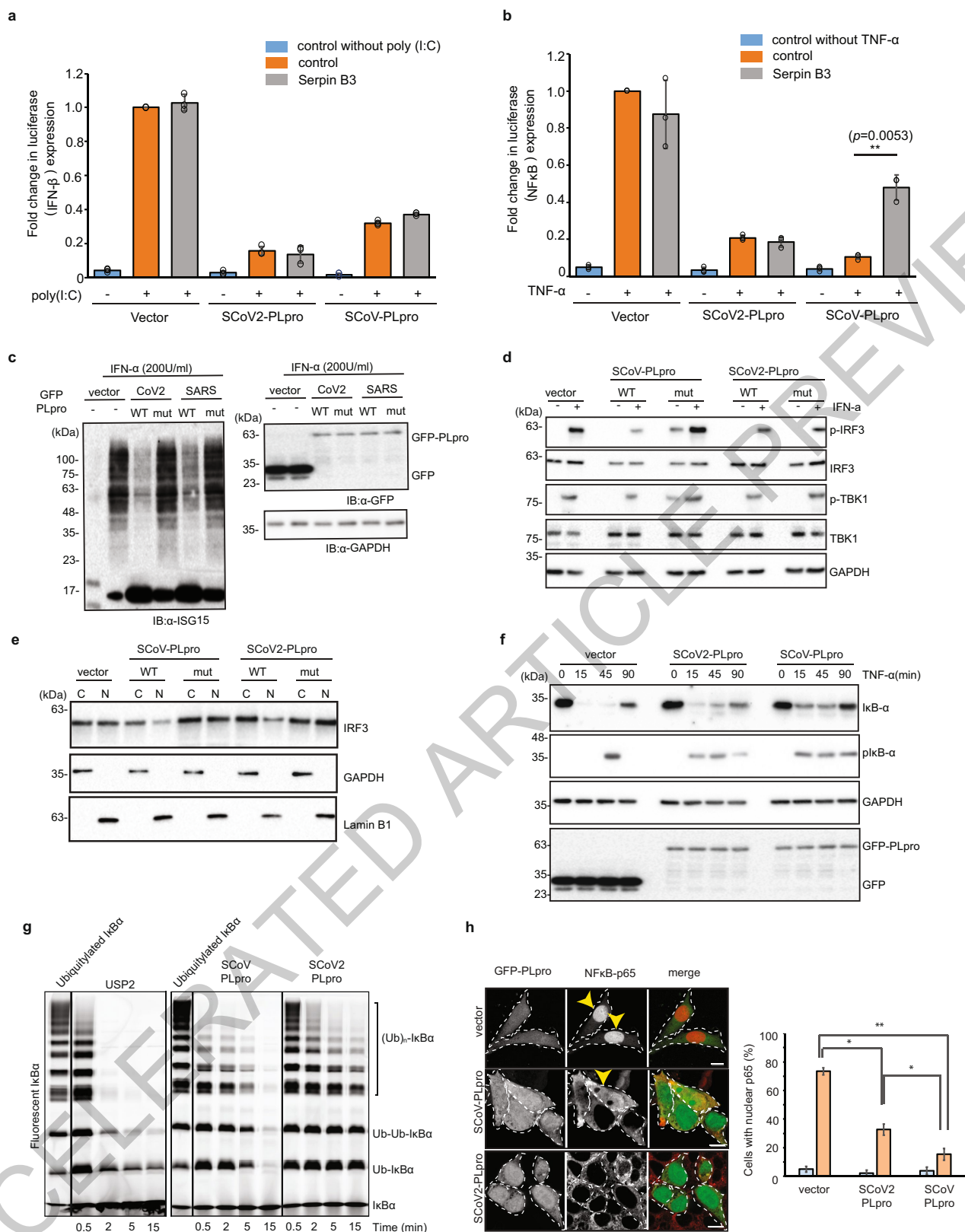
Article

Extended Data Fig. 4 | Structural analysis of GRL-0167, SCoV2-PLpro complex.

a, Structural model of GRL-0617 bound SCoV2-PLpro. The conformation of Tyr268 on SCoV2-PLpro and the coordinates of GRL-0617 is obtained from the SCoV-PLpro:GRL-0617 structure (PDB: 3E9S¹⁷). **b**, Snapshots of SCoV-PLpro (light cyan) and SCoV2-PLpro (light pink) with bound GRL-0617 (dark colors) after 1 μ s of molecular dynamics simulation. The protein backbones are shown in cartoon representation, and the ligand with contacting residues as sticks. **c**, RMSD of the GRL-0617 bound to SCoV-PLpro (light blue) and SCoV2-PLpro (light pink) as a function of time. The RMSD was calculated for non-hydrogen atoms of GRL-0617 with respect to the starting structures in the MD simulations after superimposing the helix backbone atoms of PLpro. **d**, In vitro PLpro inhibition assay. Initial velocity of AMC release from ubiquitin-AMC in different concentration of GRL-0617 was measured and normalized to DMSO control. IC₅₀ of GRL-0617 to SCoV-PLpro and SCoV2-PLpro

were presented. Data are presented as mean \pm S.D (n=3, independent experiments). **e**, In vitro PLpro inhibition assay. Initial velocity of AMC release from ISG15-AMC in different concentration of GRL-0617 was measured and normalized to DMSO control. IC₅₀ of GRL-0617 to SCoV-PLpro were presented. Data are presented as mean \pm S.D (n=3, independent experiments). **f**, Effects of GRL-0617 on (left) delISGylase or (right) deubiquitinase activity of PLpro of SARS and SARS-CoV-2. **g**, Effects of GRL-0617 on SCoV-PLpro activity to (left) ubiquitin or (right) K48-Ub₂ propargyl activity-based probes. Inhibitory effect of GRL-0617 on ubiquitin species was tested with various concentration of GRL-0617 (0-400 μ M). **h**, Effects of GRL-0617 on SCoV2-PLpro activity to (left) ISG15-C_{term} or (right) ISG15 propargylamide activity-based probes. Inhibitory effect of GRL-0617 on ISG15 was tested with various concentration of GRL-0617 (0-400 μ M). Experiments in **f-h** were repeated three times independently with similar results.

ACCELERATED ARTICLE PREVIEW



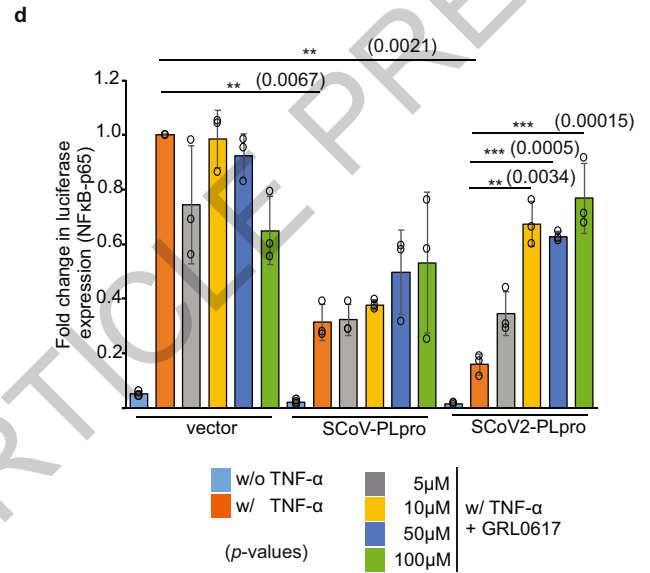
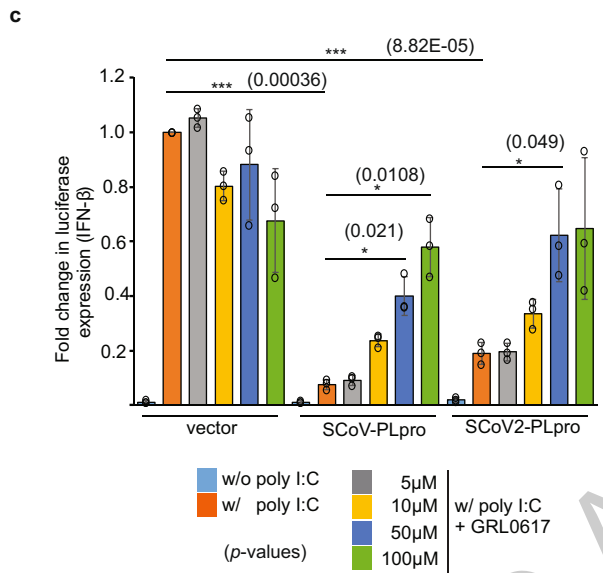
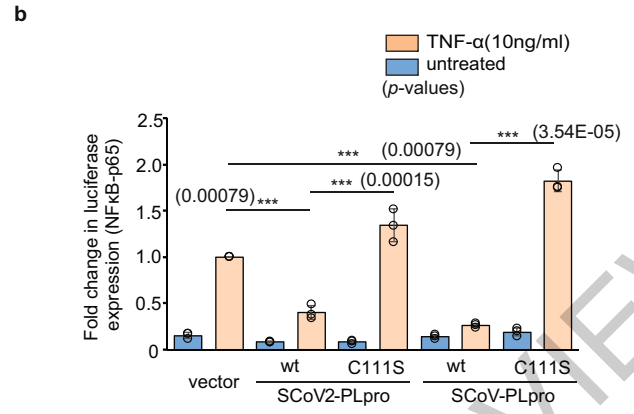
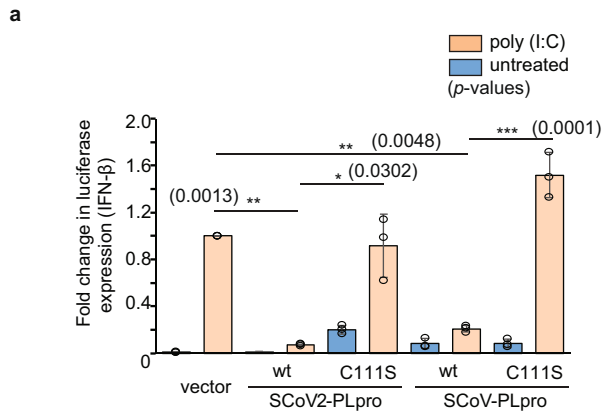
Extended Data Fig. 5 | See next page for caption.

Article

Extended Data Fig. 5 | Physiological roles of PLpro in cells. a, b, Effect of SERPIN B3 on PLpro mediated (a) IFN- β or (b) NF- κ B p65 expression level. A549 Cells were co-transfected with indicated GFP-PLpro and Myc-SERPINS and treated with either poly (I:C) or TNF- α to induce IFN- β and NF- κ B p65 expression, respectively. Fold changes of luciferase level are presented. **c,** Effect of PLpro on IFN-induced cellular ISGylation. A549 cells were transfected with indicated PLpro plasmids and treated with IFN- α . Lysates were analysed by immune-blotting with indicated antibodies. **d, e** Effect of PLpro on IFN-signalling pathway. **d,** A549 cells were transfected with indicated PLpro plasmids and treated with IFN- α . Lysates were analysed by immune-blotting with indicated antibodies. **e,** Effect of PLpro on cellular localization of IRF3. Cells from (d) were fractionated into cytosol and nucleus and the level of IRF3

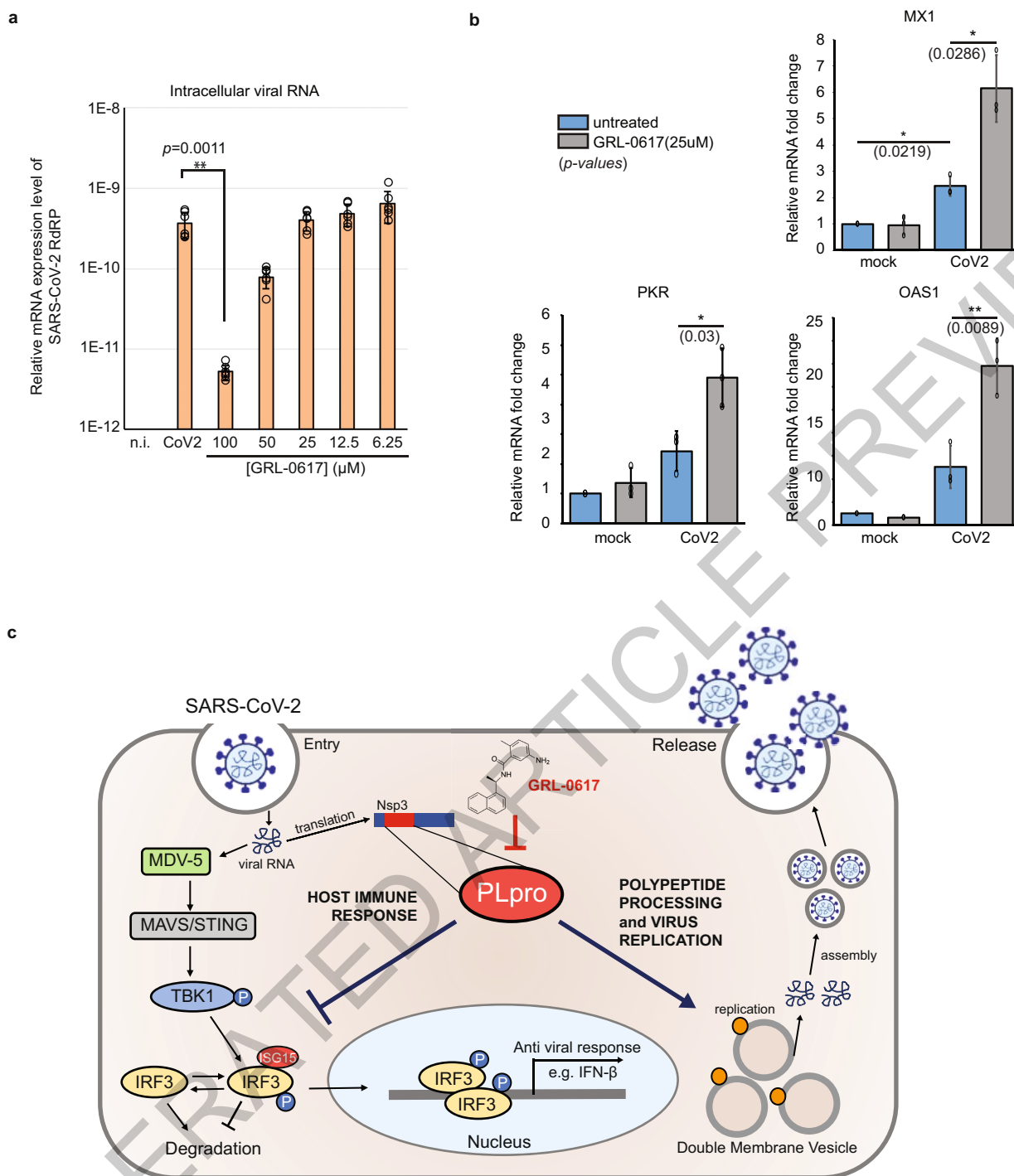
was analysed. Lamin B1 was used for nuclear fraction control. **f,** Effect of PLpro on the NF- κ B pathway. I κ B- α phosphorylation and degradation were examined from A549 cells expressing indicated GFP-PLpro under treatment of TNF- α . **g,** *in vitro* I κ B α deubiquitylation assay. Ubiquitinated I κ B α were incubated with SCoV-PLpro or SCoV2-PLpro. USP2 were used as positive control. **h,** Effect of PLpro on NF- κ B p65 cellular localization. Scale bar = 10 μ m. Data in **a, b, h** are presented as mean \pm S.D (n=3, independent experiments). * $p < 0.05$, ** $p < 0.01$; two-tailed paired t-tests. Experiments in **c-h** were repeated three times independently with similar results. **e,** Effect of PLpro on the NF- κ B pathway. I κ B- α phosphorylation and degradation were examined from A549 cells expressing indicated GFP-PLpro under treatment of TNF- α .

ACCELERATED ARTICLE PREVIEW



Extended Data Fig. 6 | Effect of PLpro on IFN-β or NF-κB p65 expression level. a, b, Effect of PLpro on (a) IFN-β or (b) NF-κB p65 expression level. A549 Cells were transfected with indicated GFP-PLpro and treated with either poly (I:C) or TNF-α to induce IFN-β and NF-κB p65 expression, respectively. **c, d,** Effect of GRL-0617 on PLpro mediated (c) IFN-β or (d) NF-κB p65 expression

level. A549 Cells were transfected with indicated GFP-PLpro and treated with either poly (I:C) or TNF-α to induce IFN-β and NF-κB p65 expression, respectively. GRL-0617 is treated as indicated. All Data are presented as mean ± S.D (n=3, independent experiments). **p* < 0.05, ***p* < 0.01, ****p* < 0.001; two-tailed paired t-tests.



Extended Data Fig. 7 | Inhibitory effects of GRL-0617 on SARS-CoV2 infection. **a**, Intracellular virus production was analysed by PCR targeting SARS-CoV-2 RdRP mRNA. Relative expression level of SARS-CoV2-2 genomic RNA was normalized to cellular GAPDH level. **b**, Intracellular RNA was isolated from cells without infection or cells infected with SARS-CoV-2 with or without treatment of GRL-0617. Relative mRNA-level fold change of indicated genes

were analysed in a qRT-PCR analysis and normalized to ACTB levels. Data in **a**, **b** are presented as mean \pm S.D (n=3, independent experiments). * $p < 0.05$, ** $p < 0.01$; two-tailed paired t-tests. **c**, Schematic representation of the role of SARS-CoV-2 PLpro in the viral life cycle. The physiological role of SCoV2-PLpro in both host-immune response and polypeptide processing is shown. Inhibition of PLpro by GRL-0617 is also presented.

Extended Data Table 1 | Data collection and refinement statistics (molecular replacement)

SCoV2-PLpro (C111S): mISG15 (PDB: 6YVA)

Data collection

Space group	P 62 2 2
Cell dimensions	
<i>a</i> , <i>b</i> , <i>c</i> (Å)	157.047, 157.047, 83.633
α , β , γ (°)	90, 90, 120
Resolution (Å)	45.34 – 3.185 (3.298 - 3.185) [†]
<i>R</i> _{sym} or <i>R</i> _{merge}	0.05751 (0.5689)
<i>I</i> / σ <i>I</i>	8.58 (1.19)
Completeness (%)	99.61 (97.77)
Redundancy	2.0 (2.0)

Refinement

Resolution (Å)	45.34 – 3.185 (3.298 - 3.185)
No. reflections	10590 (1008)
<i>R</i> _{work} / <i>R</i> _{free}	0.2496 / 0.2902
No. atoms	3407
Protein	3383
Ligand/ion	1
Water	23
<i>B</i> -factors	87.60
Protein	87.72
Ligand/ion	167.02
Water	66.67
R.m.s. deviations	
Bond lengths (Å)	0.004
Bond angles (°)	0.65

Statistics for data collection and refinement are presented. * A single crystal was used for data collection and structure determination. [†]Values in parentheses are for highest-resolution shell.

Extended Data Table 2 | Kinetic parameters on AMC substrates

Kinetic Parameter		Triazole-linked K48-Ub ₂ -AMC	ISG15-AMC
SARS-CoV-2 PLpro	Apparent k_{cat}/K_M [$M^{-1}s^{-1}$]	2.41 ± 0.94 (E+05)	5.21 ± 0.36 (E+05)
	k_{cat} [s^{-1}]	14.75 ± 3.28	4.43 ± 0.13
	K_M [μM]	61.23 ± 19.76	8.50 ± 0.54
	Michaelis-Menten curve fit (R^2)	0.9914	0.9987
SARS PLpro	Apparent k_{cat}/K_M [$M^{-1}s^{-1}$]	13.94 ± 3.50 (E+05)	5.31 ± 0.56 (E+05)
	k_{cat} [s^{-1}]	62.9 ± 8.45	11.89 ± 0.75
	K_M [μM]	45.13 ± 9.57	22.41 ± 1.89
	Michaelis-Menten curve fit (R^2)	0.9911	0.9997
mUSP18	Apparent k_{cat}/K_M [$M^{-1}s^{-1}$]		0.68 ± 0.07 (E+05)
	k_{cat} [s^{-1}]	N.D.	0.06 ± 0.002
	K_M [μM]		0.89 ± 0.093
	Michaelis-Menten curve fit (R^2)		0.9895

Kinetic parameters for SCoV-PLpro, SCoV2-PLpro and murineUSP18 to triazole-linked K48-Ub₂-AMC or ISG15-AMC are presented. Values are presented as mean \pm S.D (n=3, independent experiments).

Extended Data Table 3 | Binding kinetics of PLpro to K48-Ub₂ or ISG15

		$k_{on} \pm \text{S.E.M}^a$ ($10^2 \text{ M}^{-1}\text{s}^{-1}$)	$k_{off} \pm \text{S.E.M}^a$ (10^{-1} s^{-1})	$K_d \pm \text{S.E.M}^a$ (μM)	R^{2b}
CoV2	Triazole linked K48-Ub ₂	158 ± 8.00	4.30 ± 0.11	27.28 ± 1.55	0.99
PLpro	Human ISG15	1530 ± 52.4	2.15 ± 0.06	1.41 ± 0.06	0.99
	Mouse ISG15	122 ± 4.48	0.20 ± 0.02	1.64 ± 0.17	0.97
SARS PLpro	Triazole linked K48-Ub ₂	820 ± 32.1	0.81 ± 0.02	0.99 ± 0.04	0.98
	Human ISG15	88.8 ± 14.5	0.76 ± 0.06	8.60 ± 1.56	0.98
	Mouse ISG15	24.7 ± 0.75	0.23 ± 0.01	9.34 ± 0.41	0.98

Binding kinetic parameters for SCoV-PLpro, SCoV2-PLpro to triazole-linked K48-Ub₂, humanISG15 or mouseISG15 are presented. Values are presented as mean ± S.E.M. (n=3, independent experiments). ^a S.E.M., standard error of mean. ^b R², goodness of the curve fit between experimental data and mathematical 1:1 binding curve

Reporting Summary

Nature Research wishes to improve the reproducibility of the work that we publish. This form provides structure for consistency and transparency in reporting. For further information on Nature Research policies, see [Authors & Referees](#) and the [Editorial Policy Checklist](#).

Statistics

For all statistical analyses, confirm that the following items are present in the figure legend, table legend, main text, or Methods section.

n/a Confirmed

- | | | |
|-------------------------------------|-------------------------------------|--|
| <input type="checkbox"/> | <input checked="" type="checkbox"/> | The exact sample size (n) for each experimental group/condition, given as a discrete number and unit of measurement |
| <input type="checkbox"/> | <input checked="" type="checkbox"/> | A statement on whether measurements were taken from distinct samples or whether the same sample was measured repeatedly |
| <input type="checkbox"/> | <input checked="" type="checkbox"/> | The statistical test(s) used AND whether they are one- or two-sided
<i>Only common tests should be described solely by name; describe more complex techniques in the Methods section.</i> |
| <input checked="" type="checkbox"/> | <input type="checkbox"/> | A description of all covariates tested |
| <input checked="" type="checkbox"/> | <input type="checkbox"/> | A description of any assumptions or corrections, such as tests of normality and adjustment for multiple comparisons |
| <input type="checkbox"/> | <input checked="" type="checkbox"/> | A full description of the statistical parameters including central tendency (e.g. means) or other basic estimates (e.g. regression coefficient) AND variation (e.g. standard deviation) or associated estimates of uncertainty (e.g. confidence intervals) |
| <input type="checkbox"/> | <input checked="" type="checkbox"/> | For null hypothesis testing, the test statistic (e.g. F , t , r) with confidence intervals, effect sizes, degrees of freedom and P value noted
<i>Give P values as exact values whenever suitable.</i> |
| <input checked="" type="checkbox"/> | <input type="checkbox"/> | For Bayesian analysis, information on the choice of priors and Markov chain Monte Carlo settings |
| <input checked="" type="checkbox"/> | <input type="checkbox"/> | For hierarchical and complex designs, identification of the appropriate level for tests and full reporting of outcomes |
| <input checked="" type="checkbox"/> | <input type="checkbox"/> | Estimates of effect sizes (e.g. Cohen's d , Pearson's r), indicating how they were calculated |

Our web collection on [statistics for biologists](#) contains articles on many of the points above.

Software and code

Policy information about [availability of computer code](#)

Data collection	<input type="text" value="Image lab software 5.2.1"/>
Data analysis	<input type="text" value="Image lab software 5.2.1 ,Prism5, MaxQuant 1.6.5, Perseus 1.6.5, Pymol (1.7.6.0), phenix (1.17.1-3660), ccp4 (7.0.078), coot (0.8.9.2), Modeller (9.24), Gromacs (2019.6)"/>

For manuscripts utilizing custom algorithms or software that are central to the research but not yet described in published literature, software must be made available to editors/reviewers. We strongly encourage code deposition in a community repository (e.g. GitHub). See the Nature Research [guidelines for submitting code & software](#) for further information.

Data

Policy information about [availability of data](#)

All manuscripts must include a [data availability statement](#). This statement should provide the following information, where applicable:

- Accession codes, unique identifiers, or web links for publicly available datasets
- A list of figures that have associated raw data
- A description of any restrictions on data availability

The atomic coordinates of PLpro-ISG15 (murine) have been deposited in the PDB with accession code 6YVA in the Protein Data Bank. The mass spectrometry proteomics data have been deposited to the ProteomeXchange Consortium⁷³ via the PRIDE partner repository⁷⁴ with the dataset identifier PXD018983. The papain-like protease domain sequence is obtained from SARS-CoV-2 complete genome (NCBI genome databank, Severe acute respiratory syndrome coronavirus 2 isolate Wuhan-Hu-1, complete genome; NC_045512). Protein sequence for CoV2 PLpro-Ubl domain (amino acids, 746-1060) of Nsp3 protein from SARS-CoV-2 (Nsp3; YP_009725299.1). Full gel images can be found in Supplementary Figure 1 and source data that support this study and can be found in Supplementary Information. Any other relevant data are available from the corresponding authors upon reasonable request.

Field-specific reporting

Please select the one below that is the best fit for your research. If you are not sure, read the appropriate sections before making your selection.

Life sciences Behavioural & social sciences Ecological, evolutionary & environmental sciences

For a reference copy of the document with all sections, see [nature.com/documents/nr-reporting-summary-flat.pdf](https://www.nature.com/documents/nr-reporting-summary-flat.pdf)

Life sciences study design

All studies must disclose on these points even when the disclosure is negative.

Sample size	No sample size calculation was done. Experiments were repeated three times with similar results and sample size was chosen based on the consistency and significance of measured differences between groups. We have not mentioned any differences between groups if there the differences are not statistically significant.
Data exclusions	No data were excluded from analysis.
Replication	We have repeated each experiment in the manuscript at least three times to ensure consistent results.
Randomization	No randomization was necessary as various infection samples were recorded and analyzed by a computer software for extracting the significant differences.
Blinding	Blinding was not relevant for the experiments done as various infection samples were analyzed by a computer software for extracting the significant differences.

Reporting for specific materials, systems and methods

We require information from authors about some types of materials, experimental systems and methods used in many studies. Here, indicate whether each material, system or method listed is relevant to your study. If you are not sure if a list item applies to your research, read the appropriate section before selecting a response.

Materials & experimental systems

n/a	Involved in the study
<input type="checkbox"/>	<input checked="" type="checkbox"/> Antibodies
<input type="checkbox"/>	<input checked="" type="checkbox"/> Eukaryotic cell lines
<input checked="" type="checkbox"/>	<input type="checkbox"/> Palaeontology
<input checked="" type="checkbox"/>	<input type="checkbox"/> Animals and other organisms
<input checked="" type="checkbox"/>	<input type="checkbox"/> Human research participants
<input checked="" type="checkbox"/>	<input type="checkbox"/> Clinical data

Methods

n/a	Involved in the study
<input checked="" type="checkbox"/>	<input type="checkbox"/> ChIP-seq
<input checked="" type="checkbox"/>	<input type="checkbox"/> Flow cytometry
<input checked="" type="checkbox"/>	<input type="checkbox"/> MRI-based neuroimaging

Antibodies

Antibodies used	Ubiquitin (Cat# 3936S, Provider: Cell signaling Technology, 1:2000), ISG15 (Cat# HPA004627, Sigma Aldrich/Merck, 1:1000), GAPDH (Cat# 2118, Cell signaling Technology, 1:2000), GFP trap beads (Cat #: gta-100, Provider: ChromoTek), GFP (Cat# sc-9996, Santa Cruz Biotechnology, 1:2000), IRF3 (Cat# 4302, Cell signaling Technology, 1:2000), phospho-IRF3(Ser396) (Cat# 4947, Cell signaling Technology, 1:1000), IκBα (Cat# 4812, Cell signaling Technology, 1:2000), phospho-IκBα(Ser32/36) (Cat# 9246, Cell signaling Technology, 1:1000), TBK1 (Cat# 3013, Cell signaling Technology, 1:2000), pTBK1 (Cat # 3300-1 Epitomics, 1:1000), P65 (NFκB) (Cat# 8008, Santa Cruz Biotechnology, 1:2000), Lamin B1 (Cat# sc-373918, Santa Cruz Biotechnology, 1:2000).
Validation	<p>Ubiquitin (Cat# 3936S, Provider: Cell signaling Technology) Validation statement from the manufacturer: Ubiquitin (P4D1) Mouse mAb detects ubiquitin, polyubiquitin and ubiquitinated proteins. This antibody may cross-react with recombinant NEDD8. Validation found at provider's website: https://www.cellsignal.com/products/primary-antibodies/ubiquitin-p4d1-mouse-mab/3936</p> <p>ISG15 (Cat# HPA004627, Sigma Aldrich/Merck) Validation statement from the manufacturer: species reactivity-human, validation-recombinant expression, orthogonal RNA seq Validation found at provider's website: https://www.sigmaaldrich.com/catalog/product/sigma/hpa004627?lang=en&region=DE</p> <p>GAPDH (Cat# 2118, Cell signaling Technology) Validation statement from the manufacturer: GAPDH (14C10) Rabbit mAb detects endogenous levels of total GAPDH protein. Species Reactivity: Human, Mouse, Rat, Monkey, Bovine, Pig Validation found at provider's website: https://www.cellsignal.com/products/primary-antibodies/gapdh-14c10-rabbit-mab/2118</p>

GFP trap beads (Cat #: gta-100, Provider: ChromoTek) Validation statement from the manufacturer: GFP-Trap® Agarose is an affinity resin for immunoprecipitation of GFP-fusion proteins. It consists of a GFP Nanobody/ VHH coupled to agarose beads. Validation found at provider's website: https://www.chromotek.com/products/detail/product-detail/gfp-trap-agarose/
GFP (Cat# sc-9996, Santa Cruz Biotechnology) Validation statement from the manufacturer: Anti-GFP Antibody (B-2) is a mouse monoclonal IgG2a (kappa light chain) GFP antibody provided at 200 µg/ml, raised against amino acids 1-238 representing full length GFP (green fluorescent protein) of Aequorea victoria origin Validation found at provider's website: https://www.scbt.com/p/gfp-antibody-b-2?productCanUrl=gfp-antibody-b-2&_requestid=272661
IRF3 (Cat# 4302, Cell signaling Technology) Validation statement from the manufacturer: IRF-3 (D83B9) Rabbit mAb detects endogenous levels of total IRF-3 protein. Species Reactivity:Human, Mouse, Rat, Monkey Validation found at provider's website: https://www.cellsignal.com/products/primary-antibodies/irf-3-d83b9-rabbit-mab/4302
phospho-IRF3(Ser396) (Cat# 4947, Cell signaling Technology) Validation statement from the manufacturer: phospho-IRF-3 (Ser396) (4D4G) Rabbit mAb detects endogenous levels of IRF-3 when phosphorylated at Ser396. Species Reactivity:Human, Mouse Validation found at provider's website: https://www.cellsignal.com/products/primary-antibodies/phospho-irf-3-ser396-4d4g-rabbit-mab/4947
IκBα (Cat# 4812, Cell signaling Technology) Validation statement from the manufacturer: IκBα (44D4) Rabbit mAb detects endogenous levels of total IκBα protein.Species Reactivity:Human, Mouse, Rat, Hamster, Monkey, Mink Validation found at provider's website: https://www.cellsignal.com/products/primary-antibodies/ikba-44d4-rabbit-mab/4812
phospho-IκBα(Ser32/36) (Cat# 9246, Cell signaling Technology) Validation statement from the manufacturer: Phospho-IκBα (Ser32/36) (5A5) Mouse mAb detects endogenous levels of IκBα only when phosphorylated at Ser32/36.Species Reactivity: Human, Mouse, Rat, Monkey Validation found at provider's website: https://www.cellsignal.com/products/primary-antibodies/phospho-ikba-ser32-36-5a5-mouse-mab/9246
TBK1 (Cat# 3013, Cell signaling Technology) Validation statement from the manufacturer: TBK1 Antibody detects endogenous levels of total TBK1/NAK protein.Species Reactivity:Human, Mouse, Rat, Monkey Validation found at provider's website: https://www.cellsignal.com/products/primary-antibodies/tbk1-nak-antibody/3013
pTBK1 (Cat # ab109272 abcam) Validation statement from the manufacturer: This antibody only detects NAK/TBK1 phosphorylated at serine 172.Validation found at provider's website: https://www.abcam.com/naktbk1-phospho-s172-antibody-epr28672-ab109272.html
P65(NFκB) (Cat# 8008, Santa Cruz Biotechnology) Validation statement from the manufacturer: Anti-NFκB p65 Antibody (F-6) is a mouse monoclonal IgG1 (kappa light chain) NFκB p65 antibody provided at 200 µg/ml, raised against amino acids 1-286 mapping at the N-terminus of NFκB p65 of human origin Validation found at provider's website: https://www.scbt.com/p/nfkappab-p65-antibody-f-6?productCanUrl=nfkappab-p65-antibody-f-6&_requestid=285577
Lamin B1 (Cat# sc-373918, Santa Cruz Biotechnology) Validation statement from the manufacturer: Lamin B1 Antibody (G-1) is a mouse monoclonal IgG3 (kappa light chain) provided at 200 µg/ml, specific for an epitope mapping between amino acids 559-586 at the C-terminus of Lamin B1 of mouse origin Validation found at provider's website: https://www.scbt.com/p/lamin-b1-antibody-g-1?requestFrom=search

Eukaryotic cell lines

Policy information about [cell lines](#)

Cell line source(s)	A549 cells (ATCC® CCL-185™), HeLa (ATCC® CCL-2™), CaCo-2 (DSMZ, ACC 169)
Authentication	Cell lines were authenticated using STR DNA profiling.
Mycoplasma contamination	All the cell lines used tested negative for mycoplasma.
Commonly misidentified lines (See ICLAC register)	The cell lines used in the study are not in the commonly misidentified lines list.